

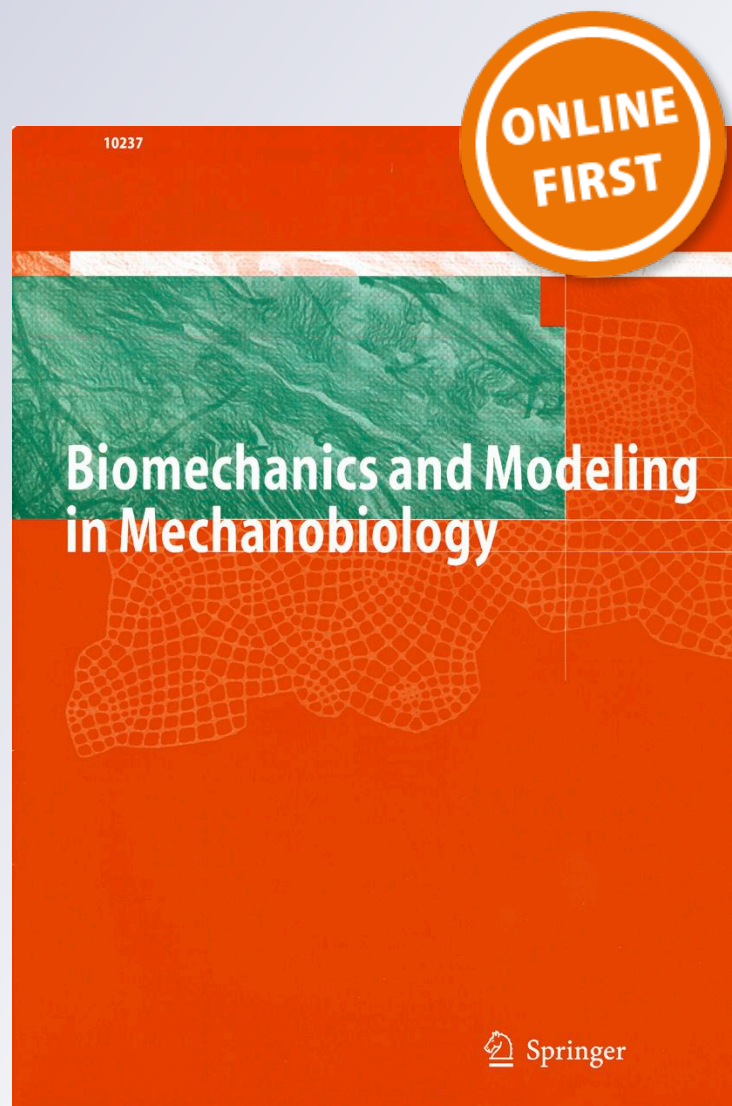
Mechanics of blast loading on the head models in the study of traumatic brain injury using experimental and computational approaches

S. Ganpule, A. Alai, E. Plougonven & N. Chandra

**Biomechanics and Modeling in
Mechanobiology**

ISSN 1617-7959

Biomech Model Mechanobiol
DOI 10.1007/s10237-012-0421-8



Your article is protected by copyright and all rights are held exclusively by Springer-Verlag. This e-offprint is for personal use only and shall not be self-archived in electronic repositories. If you wish to self-archive your work, please use the accepted author's version for posting to your own website or your institution's repository. You may further deposit the accepted author's version on a funder's repository at a funder's request, provided it is not made publicly available until 12 months after publication.

Mechanics of blast loading on the head models in the study of traumatic brain injury using experimental and computational approaches

S. Ganpule · A. Alai · E. Plougonven · N. Chandra

Received: 20 December 2011 / Accepted: 10 July 2012
© Springer-Verlag 2012

Abstract Blast waves generated by improvised explosive devices can cause mild, moderate to severe traumatic brain injury in soldiers and civilians. To understand the interactions of blast waves on the head and brain and to identify the mechanisms of injury, compression-driven air shock tubes are extensively used in laboratory settings to simulate the field conditions. The overall goal of this effort is to understand the mechanics of blast wave–head interactions as the blast wave traverses the head/brain continuum. Toward this goal, surrogate head model is subjected to well-controlled blast wave profile in the shock tube environment, and the results are analyzed using combined experimental and numerical approaches. The validated numerical models are then used to investigate the spatiotemporal distribution of stresses and pressure in the human skull and brain. By detailing the results from a series of careful experiments and numerical simulations, this paper demonstrates that: (1) Geometry of the head governs the flow dynamics around the head which in turn determines the net mechanical load on the head. (2) Bio-mechanical loading of the brain is governed by direct wave transmission, structural deformations, and wave reflections from tissue–material interfaces. (3) Deformation and stress analysis of the skull and brain show that skull flexure and tissue cavitation are possible mechanisms of blast-induced traumatic brain injury.

Keywords Blast · TBI · Head · Mechanics · Experiments · Numerical models · FSI

1 Introduction

Improvised explosive devices (IEDs) are weapons frequently utilized by insurgents in Iraq and Afghanistan; the explosive forces generated from these IEDs can cause traumatic brain injury (TBI), recognized as the “signature wound” in these conflicts. The 15 point Glasgow Coma Scale (GCS) (Teasdale and Jennett 1974) defines the severity of a TBI as mild (13–15), moderate (9–12), severe (3–8), and vegetative state (<3). A recent RAND report estimates that 20 % of the deployed force (total deployed 1.6 million) in these conflicts potentially suffers from TBI; 40–60 % of these injuries are categorized as mild and occur due to explosion-induced blast waves (Tanielian and Jaycox 2008). It is speculated that blast-induced traumatic brain injury (bTBI) is a stress wave dominated phenomenon as opposed to a rotational acceleration/deceleration-induced injury, typically associated with the impact injuries commonly encountered in sports and automobile accidents (Courtney and Courtney 2009; Grujicic et al. 2011; Moore et al. 2009; Moss et al. 2009; Nyein et al. 2010; Taylor and Ford 2009). Our current understanding of the specific loading pathways and mechanisms of blast-induced neurotrauma (BINT) remains incomplete (Ling et al. 2009). This is particularly detrimental to medical personnel and patients, since often times bTBI (especially mild and moderate) goes undetected with no diagnosis available through neuroradiology or neurophysiology; psychological examination may or may not be able to reveal this ailment (Desmoulin and Dionne 2009; Elder and Cristian 2009). Repeated exposure to the blast can have cumulative effects with irreversible damage to a soldier’s mental capacity

Electronic supplementary material The online version of this article (doi:10.1007/s10237-012-0421-8) contains supplementary material, which is available to authorized users.

S. Ganpule · A. Alai · E. Plougonven · N. Chandra (✉)
Department of Mechanical and Materials Engineering, University
of Nebraska–Lincoln, Lincoln, NE, 68588-0656, USA
e-mail: nchandra2@unl.edu

(Wang et al. 2011). Detailed knowledge of the mechanics of blast wave–head interactions is important to the basic understanding of bTBI. The overall goal of this effort is to understand blast wave–head interactions through an integrated experimental–computational approach. Through this approach, we hope to identify the mechanics of biomechanical loading of the head and the brain as the blast wave traverses the head/brain continuum.

While establishing mechanisms of bTBI, it is important to accurately reproduce field conditions. While blast explosions can result in primary (pure blast), secondary (interaction with shrapnel or fragments), tertiary (impact with environmental structures), or/and quaternary (toxic gases) effects (DePalma et al. 2005; Moore et al. 2008), in this work, we focus on the effect of primary blast. Furthermore, we consider blast parameters which are likely in the range of mild blast traumatic brain injury (mbTBI). For example, when IEDs detonate, at sufficient distances, they propagate as blast waves with a shock front; it is these waves that interact with the head/body causing mbTBI. We will refer to these blast waves with a shock front traveling at supersonic speed, followed by an exponential decay in pressure simply as *blast waves*, without the loss of generality. Where the incidence of mbTBI becomes possible, blast waves are in a planar form and can be characterized as Friedlander waves. Shock tubes, when designed correctly and tested properly, can accurately simulate these free-field explosions.

In this work, we use a specially designed compression-driven air shock tube to replicate free-field blast conditions and expose a surrogate head to a well-defined Friedlander wave. The interactions between the blast wave and the surrogate head are modeled using nonlinear finite element model based on Coupled Eulerian Lagrangian formulation; the numerical results are compared with the experimental data for model validation. The various aspects of the mechanics of the blast wave–head interactions are analyzed and characterized. In order to understand blast wave–human head interactions and analyze how the blast loading affects the contents of the brain, experimental boundary conditions are applied to an anatomically accurate human head-brain numerical model. Together, experiments and numerical models provide valuable insight into the mechanics of blast wave propagation and the effect of anatomical features on the subsequent biomechanical loading of the head/brain complex.

In Sect. 2, we describe the experimental details of the shock tube, instrumentation/data acquisition methods, and the constructional details of the surrogate head. In this section, we also describe the finite element solution method; details of how the anatomically accurate head/brain model is built from MRI; and numerical validation method. In Sect. 3, we present experimental pressure measurements along the shock tube and at five locations on the surface of the surrogate dummy head and validation of the numerical models.

We also establish the relationship between surface pressure and the pressure $[-(\sigma_{11} + \sigma_{22} + \sigma_{33})/3]$ in the brain/skull. The results are interpreted in terms of pressure wave transmission and skull deformation. In Sect. 4, we discuss the interactions of the hydrodynamic blast flow field on a human head in terms of direct and indirect loadings and link the spatial-temporal variations of the pressure field in the brain to the arrival time analysis of the different wave fronts. The key aspects of the experimental and computational analyses are summarized in the final section.

2 Methods

2.1 Experiments

Experiments are carried out in the 711×711 mm ($28'' \times 28''$) cross-section shock tube designed and tested at the University of Nebraska–Lincoln's blast wave generation facility (Chandra et al. 2011). The four main components of the shock tube are: (1) driver, (2) transition, (3) straight/extension sections (includes test section), and (4) catch tank (Fig. 1a). The driver section contains pressurized gas (e.g., Nitrogen or Helium) which is separated from the transition by several 0.025-mm-thick Mylar membranes, while the remaining sections contain air at atmospheric pressure and at room temperature. The transition section is used to change the cross-section of the tube from a cylinder (driver section) to a square (extension sections); the square section is a design element to observe events in the test section with high speed video imaging (600,000 frames per second). Upon membrane rupture, a blast wave is generated which expands through the transition and develops into planar shock-blast waveform in the extension section(s). The test section is strategically located to expose specimens to the blast wave profile of interest (Friedlander in this case). Finally, the blast wave exits the shock tube and enters the catch tank which absorbs and releases blast wave energy and reduces the noise intensity. In addition, the catch tank is designed to reduce rarefaction waves from re-entering the shock tube. The shock tube is designed and built such that a fully developed planar shock-blast wave is obtained in the test section located approximately 2,502 mm from the driver end; the total length of the shock tube is 12,319 mm. The cross-sectional dimensions of this shock tube is designed such that a head-neck surrogate (e.g., Anthropomorphic Test Dummies (ATD's) or cadaver head) experiences a planar blast wave without significant side-wall reflections (Kleinschmit 2011). The planarity of the blast wave is verified by pressure measurements across the test section of the shock tube (Kleinschmit 2011).

The realistic explosive dummy (RED) head used as the surrogate is based on the Facial and Ocular Countermeasures Safety (FOCUS) head which is modified from the Hybrid

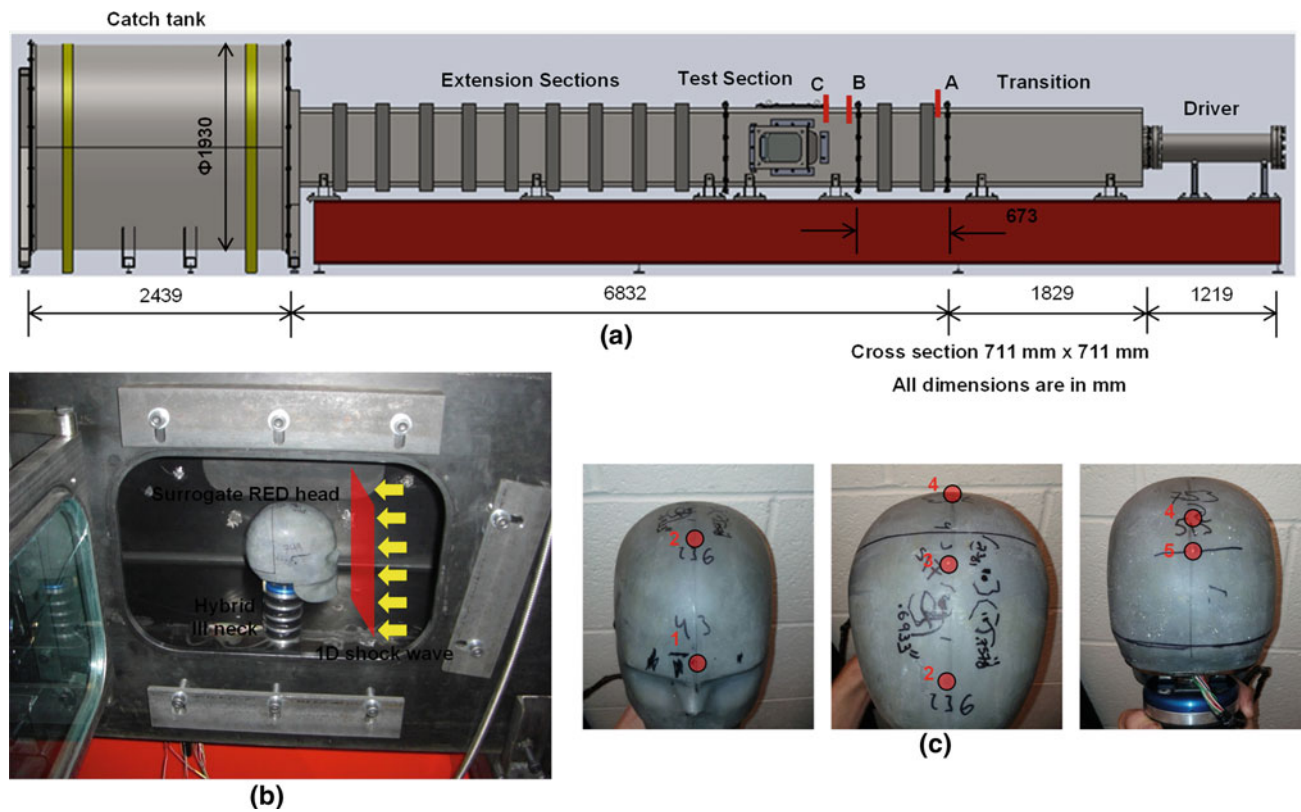


Fig. 1 Experimental setup **a** schematic of the 711 × 711 mm shock tube system **b** realistic explosive dummy (RED) head with hybrid III neck placed inside the test section of the shock tube **c** sensor locations along the midsagittal plane of the RED head

III dummy head, the latter developed for frontal impacts in automotive accidents. The external geometry of the FOCUS headform (and hence RED head) is designed to replicate a 50th percentile male soldier across the three branches of the military Army, Navy, and Air Force (Kennedy 2007). The RED head consists of a polyurethane skull with an opening for the brain and cerebrospinal fluid and is attached to the neck through the base plate. The RED head is used in conjunction with the Hybrid III neck in these experiments, and intracranial contents are not included.

The RED head assembly is placed in the test section of the shock tube as shown in Fig. 1b and is subjected to frontal blast loading. The shape, overpressure, and duration of the incident blast wave at a given location are known a priori. This is achieved through sample trials in the shock tube, conducted without the surrogate head and the neck. Surface pressures are measured at different locations on the surface of the head along the mid-sagittal plane using Kulite pressure sensors (model LE-080-250A). The sensor locations are shown in Fig. 1c. The sensing elements can measure the absolute pressure from 0 to 250 psi (0–1.72 MPa) with a nominal calibration of 0.400 mV/psi (58.02 mV/MPa) using 10 V excitation. Incident (side-on) blast wave pressures are measured at locations A, B, C (Fig. 1a) along the length of the shock tube using PCB pressure gauges (model 134A24).

All pressure sensors utilized in experiments are calibrated under shock loading conditions using a separate 101 mm (4") diameter shock tube and using a flat-topped wave. Accurate calibrations are achieved by generating precisely controlled shock wave velocities and invoking the Rankine–Hugoniot jump conditions to relate shock wave velocity to shock wave overpressures.

2.2 Computational modeling

Finite Element (FE) modeling technique is used to simulate the propagation of a planar blast wave through the shock tube, the interaction dynamics of the blast wave with the head, and the response of the head/brain to such a loading. In order to effectively use the experimental results to understand blast wave interactions with the head and its contents, the following analysis strategy is used:

- (a) A finite element based numerical model is developed for the RED (dummy) head and the shock tube, in conjunction with the Coupled Eulerian Lagrangian (CEL) formulation; here, the experimental data is used to validate the computational model in terms of surface pressure–time ($p-t$) history on the head and hence mechanical load experienced by the head. The

agreement between experiments and simulations validates the CEL formulation, solution methodology, the ability to capture the complex blast-structure flow field variables (pressure, velocities, and flow separation), as well as the resulting surface pressures on the structure and the fluid–structure interaction (FSI) effects.

- (b) Once the experimental pressure field is validated, the model is then used to numerically predict the deformation and stress fields in the brain of an anatomically accurate human head model developed from the MRI data set. The anatomically accurate human head form is additionally validated (in terms of geometry and material properties) by comparing the numerical model against a well-known blunt-impact experiment on human cadavers (Nahum et al. 1977); this assures the bio-fidelity of the human head model and the spatial–temporal accuracy of kinetic/kinematic variables in the brain tissue.

2.2.1 FE discretization

The head and neck are modeled with Lagrangian elements, and the air inside the shock tube in which the blast wave propagates is modeled with Eulerian elements (Fig. 2). The three-

dimensional human head model is generated from segmentation of high resolution MRI data obtained from the Visible Human Project (National Institutes of Health 2009). The MRI data consist of 192 T1-weighted slices of 256^2 pixels taken at 1 mm intervals in a male head. The image data are segmented into four different tissue types of the head: (1) skin, (2) skull, (3) subarachnoidal space (SAS), and (4) brain. It is not possible to separately segment cerebrospinal fluid (CSF) and structures such as membranes and bridging veins due to the resolution of the MRI data, as such they are considered a part of the SAS. The segmentation uses 3D image analysis algorithm implemented in Avizo[®]. The interface between all these tissue types are modeled as tied contact. The segmented 3D head model is imported into the meshing software HyperMesh[®] and is meshed as a triangulated surface mesh. The volume mesh is generated from this surface mesh to generate 10-noded tetrahedrons. Tetrahedron meshing algorithms are robust than hexahedral meshing algorithms and can model complex head volumes like brain and SAS faster and easier (Bourdin et al. 2007; Baker 2005; Schneiders 2000). Modified quadratic tetrahedral element (C3D10M) available in Abaqus[®] is very robust and is as good as hexahedral elements (Abaqus user's manual) as far as accuracy of results is concerned (Wieding et al. 2012; Cifuentes and Kalbag

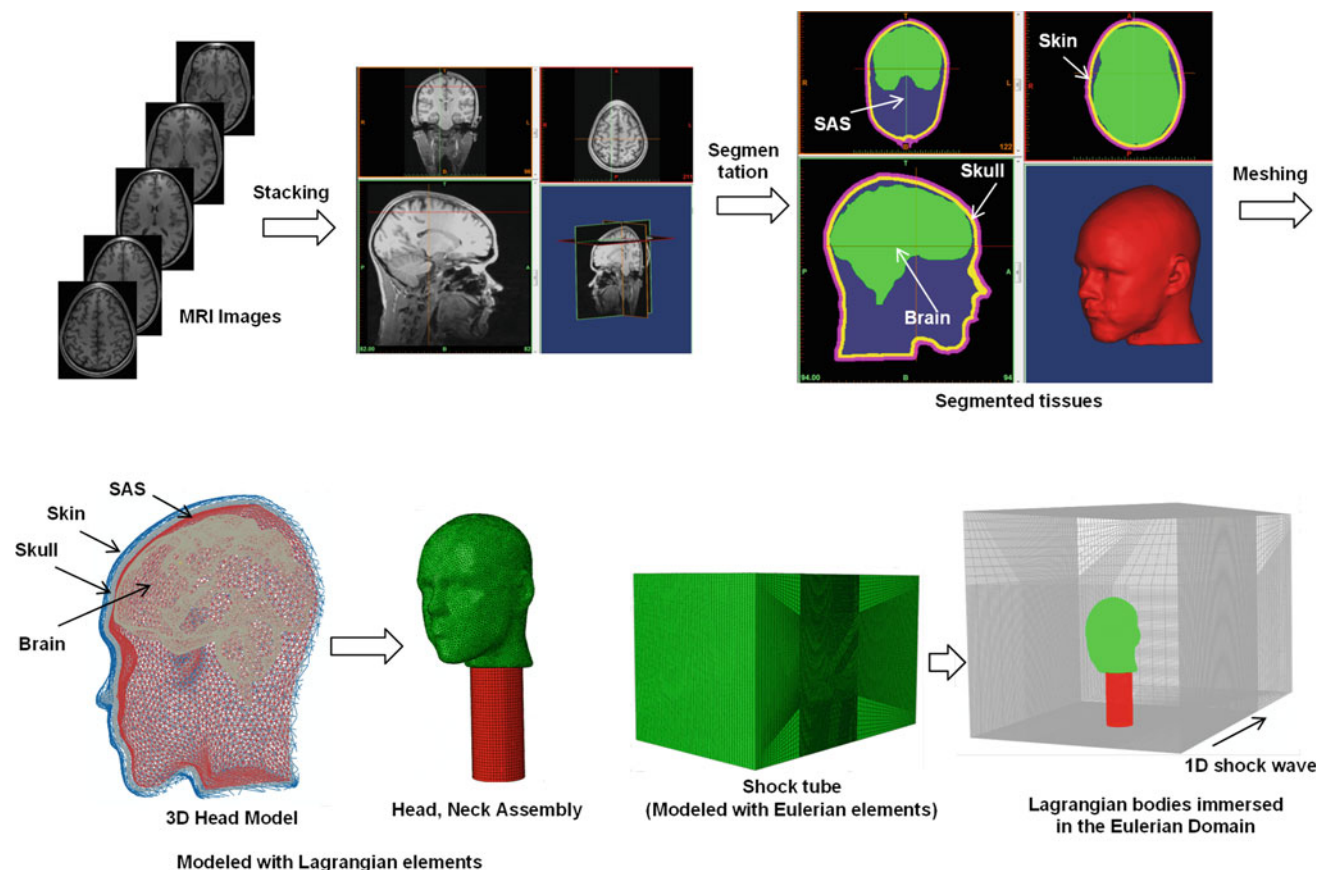


Fig. 2 Finite element (FE) discretization

Table 1 Finite element (FE) discretization

Component/tissue type	No. of nodes	No. of elements	Type of element
Skin	106,915	54,094	10 Noded tetrahedron
Skull	72,426	36,213	10 Noded tetrahedron
Subarachnoidal space (SAS)	88,783	52,198	10 Noded tetrahedron
Brain	153,750	101,781	10 Noded tetrahedron
Neck	12,691	11,340	8 Noded brick
Eulerian	1,923,390	1,870,960	8 Noded brick (Eulerian formulation)
RED head	74,856	41,057	10 Noded tetrahedron

1992; Ramos and Simões 2006). The use of specialized 3D image processing (Avizo®) and meshing software (HyperMesh®) allowed for the development of a geometrically accurate FE model. The Eulerian domain (air inside the shock tube) is meshed with eight-noded brick elements, with appropriate mesh refinement near the regions of solid bodies to capture fluid–structure interaction (FSI) effects. Parametric studies on mesh size have been performed and it is found that mesh size of 3 mm is appropriate to capture flow field around the head (i.e., pressures, velocities) and fluid–structure interaction (FSI) effects. The mesh convergence is achieved at this element size; thus, element size of 3 mm is used near the regions of solid bodies and along the direction of blast wave propagation. Table 1 shows the number of nodes, number of elements, and element types for each component of the FE model. FE discretization is schematically shown in Fig. 2. The RED head is modeled directly from the design (CAD) drawings.

2.2.2 Material models

The skin, skull, and SAS are modeled as linear, elastic, isotropic materials with properties adopted from the literature. Elastic properties in general are sufficient to capture the wave propagation characteristics for these tissue types and this approach is consistent with other published works (Chafi et al. 2010; Chen and Ostoj-Starzewski 2010; Grujicic et al. 2011; Moore et al. 2009; Moss et al. 2009; Nyein et al. 2010). The brain is modeled with an elastic volumetric response and viscoelastic shear response. The volumetric properties of the brain are taken from a recent work by Prevost et al. (2011) and the high frequency shear properties are taken from Nicolle et al. (2005). Owing to the complex anatomical structure and inherent variability associated with biological tissues, significant uncertainty is reported in material properties of the brain tissue; a comprehensive review of the brain material properties is available in Chavko et al. (2010). We believe that the material parameters for the brain used in this work are the best available combination in terms of proper testing protocols, the right range of strain rate, and data-reduction techniques for parameter estimation and applicable to high

on-set rate blast loading conditions. Furthermore, values obtained by these two studies agree well with the in vivo Magnetic Resonance Elastography (MRE) measurements (Chavko et al. 2010). Air is modeled as an ideal gas equation of state (EOS). The Mach number of the shock front from our experiments is approximately 1.4, and hence, the ideal gas EOS assumption is acceptable, as the ratio of specific heats do not change drastically at this Mach number. The material properties along with longitudinal wave speeds are summarized in Table 2.

2.2.3 Solution scheme

The finite element model is solved using the nonlinear transient dynamic procedure with the Euler-Lagrangian coupling method (Abaqus®). In this procedure, the governing partial differential equations for the conservation of momentum, mass, and energy along with the material constitutive equations and the equations defining the initial and boundary conditions are solved simultaneously. Eulerian framework allows for the modeling of highly dynamic events (e.g., shock) which would otherwise induce heavy mesh distortion. An enhanced immersed boundary method is used to provide the coupling between the Eulerian and the Lagrangian domains. Here, the Lagrangian region resides fully or partially within the Eulerian region and provides *no-flow* boundary conditions to the fluid in the direction normal to the local surface. Further, the Eulerian region provides the pressure boundary conditions to the Lagrangian region. Thus, a combination of fixed Eulerian mesh and solid–fluid interface modeling through the enhanced immersed boundary method allows for the concurrent simulations of the formation and propagation of a primary blast wave in a fluid medium and accounts for the effects of both fluid–structure interaction and structural deformations once the blast wave encounters a solid.

A typical 3D simulation requires about 7 h of CPU time on 48 dedicated Opteron parallel processors (processor speed 2.2 GHz, 2 GB memory per processor), for an integration time of 2.5 ms. The simulation time is selected such that the peaks due to stress wave action have been established. A time

Table 2 Material properties

Tissue type	Density (kg/m ³)	Young's modulus (MPa)	Poisson's ratio	Longitudinal wave speed, C_L (m/s)
(a) Elastic material properties				
Skin	1,200	16.7	0.42	188.48
Skull	1,710	5,370	0.19	1856.79
SAS	1,000	10	0.49	413.69
Neck	2,500	354	0.3	436.60
Bulk modulus (MPa)				
Brain	1,040	10	0.4999	98.07
Mode (i)	G_i (kPa)	β_i (s ⁻¹)		
(b) Viscoelastic material properties of the brain				
∞	0.27	0		
1	50	100000		
2	6.215	4350		
3	2.496	200		
4	1.228	5.3		
5	1.618	0.0051		
Density (kg/m ³)		Gas constant [J/(kg-K)]	Temperature (°C)	
(c) Ideal gas material parameters for air				
Atmospheric air	1.1607	287.05	27	

step of the order of 5×10^{-7} s is used to resolve and capture wave disturbances of the order of 1 MHz, which increases the overall computational effort for the total simulation time of interest.

2.2.4 Loading and boundary conditions

We conducted experiments on the surrogate RED head by subjecting it to blast in the frontal direction. In order to numerically reproduce the experiment, there are two possible techniques to impose the boundary conditions: technique (a) Modeling of the entire shock tube, in which driver, transition and extension sections are included in the model so that events of burst, expansion, and development of a planar of the blast wave are reproduced; technique (b) Partial model with experimentally measured ($p-t$) history is used as the pressure boundary condition, where the numerical model comprises the downstream flow field containing the test specimen. Technique (a) is computationally very expensive. For example, a full scale simulation of 711×711 mm cross-section, 9,880 mm long shock tube (excluding catch tank) with cylindrical to square transition requires about 5 million eight-noded brick Eulerian elements and takes about 147 CPU hours on a dedicated 48 processors. These simulations

reach the limits of computing power in terms of memory and simulation time. On the other hand, technique (b) requires about 1.87 million elements with 7 CPU hours. The pressure, velocity, and temperature profiles obtained using technique (b) matches well with the profiles that are obtained using full scale model [technique (a)] at the boundary and downstream locations (see supplementary material). Hence, technique (b) is capable of capturing the pressure, momentum, and energy of the shock wave and is used here to save time without scarifying accuracy. Additional details and comparison of the field variables using both these techniques are provided in the supplementary material. Approach similar to technique (b) has been widely used in shock dynamics studies using shock tubes (Honma et al. 2003; Jiang et al. 2003; Kashimura et al. 2000). The velocity perpendicular to each face of Eulerian domain (shock tube) is kept zero in order to avoid escaping/leaking of air through these faces. This will maintain a planar shock front traveling in the longitudinal direction with no lateral flow. The bottom of the neck is constrained in all six degrees of freedom to avoid rigid body motion. The tied constraint is used between the head and the neck. The interactions between Eulerian (containing air and a propagating blast wave) and Lagrangian regions are treated as fluid–solid interactions using “general contact” feature (card) in Abaqus®. In general contact, contact constraints are enforced through the penalty method

with finite sliding contact formulation. Various contact property models are available in general contact. In the present work, frictionless tangential sliding with hard contact is used as contact property model. Hard contact defines pressure–overclosure relationship between contacting surfaces. Hard contact behavior implies that: (1) the surfaces transmit no

contact pressure unless the nodes of the slave surface contact the master surface, (2) no penetration is allowed at each constraint location (for penalty constraint enforcement method used in this work, this condition is only approximated), and (3) there is no limit to the magnitude of contact pressure that can be transmitted when the surfaces are in contact.

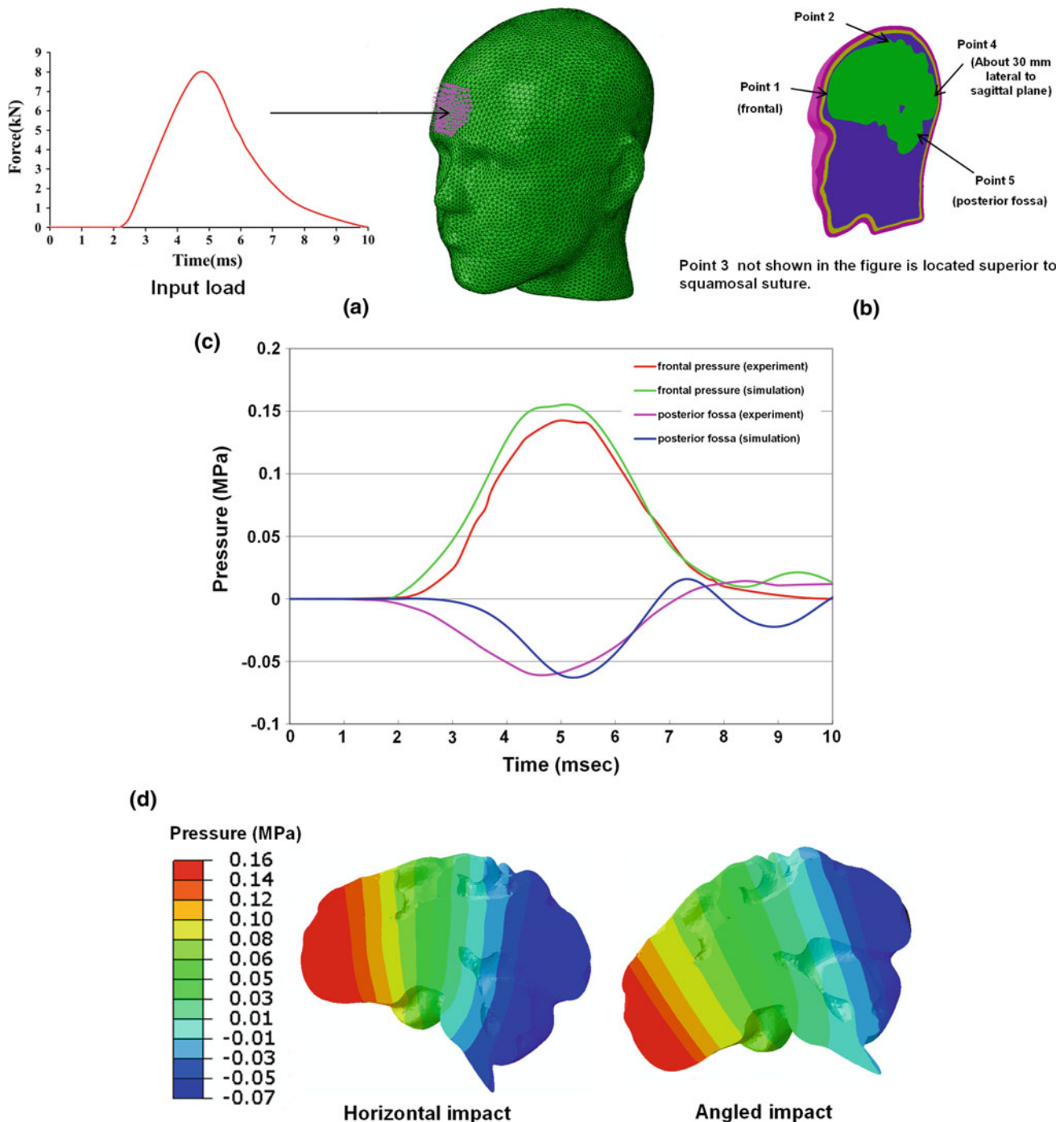


Fig. 3 Validation of MRI based head model with Nahum's experiment **a** head model subjected to Nahum's impact **b** locations at which pressure comparisons are made against experimental pressures **c** pressure–

time ($p-t$) profile comparisons at frontal and occipital locations with experimentally measured pressures **d** pressure pattern in the brain at $t = 5.1$ ms

2.2.5 Validation of the anatomically detailed computational human head model

The anatomically detailed human head model developed from the MRI data set is validated using the frontal cadaveric impact experiment of Nahum et al. (1977). Nahum's experiment has become *ade-facto* standard (Chen and Ostoj-Starzewski 2010; Claessens et al. 1997; Horgan and Gilchrist 2003; Kleiven and von Holst 2002; Ruan et al. 1994; Willinger et al. 1999; Zhang et al. 2001b; Zoghi-Moghadam and Sadegh 2009) to validate head/brain numerical models. In Nahum's experiments, seated stationary cadaver subjects were impacted at the frontal bone of the skull in the mid-sagittal plane in an anterior–posterior direction by a rigid mass traveling at a constant velocity. They measured intracranial pressure at five different locations: (1) the frontal bone adjacent to the impact contact area, (2,3) posterior and superior to the coronal and squamosal sutures, respectively, in the parietal bone, (4) inferior to the lambdoidal suture in the occipital bone and (5) in the occipital bone at the posterior fossa. To simulate Nahum's experiment, the measured impact force from the cadaver test is applied to the mid-frontal area of the numerical human head model in the anterior–posterior direction, in the form of a distributed load over an area of 1,470 mm² as shown in Fig. 3a. Pressures are measured at points corresponding to the experimental locations described above (Fig. 3b). Comparisons of pressure–time histories between model predictions and experimental measurements (test no 37) are shown in Fig. 3c and pressure pattern predicted by the brain is shown in Fig. 3d. The agreement between pressure and time ($p-t$) profiles at frontal and occipital locations is good. The pressure pattern shows typical coup–countercoup pattern, and pressure varies continuously along the sagittal plane. Similar pattern is reported by various researcher's under frontal impact loading conditions (e.g., Zhang et al. 2001b). In Nahum's experiment, head was rotated forward such that Frankfort anatomical plane was inclined 45° to the horizontal. We conducted one simulation with this angled impact (case 37), and intracranial pressures obtained are similar to one obtained with load applied in horizontal direction (Fig. 3a). The pressure pattern predicted with angled impact is shown in Fig. 3d. Table 3a shows the comparison of peak pressures and peak head accelerations between experiments and numerical simulations for various test cases of Nahum et al. (1977). Acceleration is based on resultant nodal acceleration at center of mass of the head. The agreement between experiments and numerical simulations is good for these test cases as well. The small differences in peak pressures and peak head accelerations can be attributed to the discrepancy in geometry and materials, imprecise information on neck boundary conditions and pressure transducer locations. In addition, the head model is validated against Trosseille et al. (1992); the results are shown in

Table 3 Head model validation against tests of Nahum et al. (1977)

Test no.	Input load ^a (kN)	Experiment		Simulation			% Difference (absolute)						
		Peak head acceleration (m/s ²)	Peak pressure (kPa)		Peak head acceleration ^b (m/s ²)	Peak pressure (kPa)		peak head acceleration (m/s ²)	Peak pressure (kPa)				
			Frontal	Parietal		Posterior fossa	Frontal		Parietal	Posterior fossa			
37	7.9	2,000	141.19	73.59	−60.26	2,046.94	154.5	61.93	−63.2	2.35	9.43	15.85	4.87
41	14.84	3,900	427.56	188.52	−56.80	3,857	414	186.34	−59.31	1.10	3.17	1.16	4.43
42	5.2	1,590	–	–	−43.86	1,510.74	–	–	−46.33	4.98	–	–	5.62
54	10.84	2,340	274.51	180.52	−64.39	2,393.64	247.18	141.93	−66.5	2.29	9.96	21.38	3.27

^a The stiffness of the padding material in front of the impactor for cases 37, 41, 42 and 54 is not known. Hence, for cases 41, 42, and 54, the shape of the pressure–time profile as that of case 37 is conserved. The pressure pulse is scaled to match peak input force in cases 41, 42 and 54

^b Acceleration is based on resultant nodal acceleration at center of mass of the head

Table 4 Head model validation against tests of Trosseille et al. (1992)

Test no.	Experiment Peak pressure (kPa)				Simulation Peak pressure (kPa)				% Difference (absolute)						
	Frontal	Lateral ventricle	3rd Ventricle	Occipital	Parietal	Frontal	Lateral ventricle	3rd Ventricle	Occipital	Parietal	Frontal	Lateral ventricle	3rd Ventricle	Occipital	Parietal
MS428-1	>60	30	25	-13.5	12.4	72	36.22	30.9	-17	15.2	-	20.73	23.6	25.93	22.58
MS428-2 ^a	88	40	35	-11	10.5	84	43.23	38.56	-13.5	13	4.55	8.075	10.17	22.72	23.81

^a For test No. MS428-2 acceleration time history at the center of mass as reported in Zhang et al. (2001a) is used

Table 4b. Since ventricles are not explicitly modeled in this work, the elements in the ventricle region are approximately selected based on the knowledge of head anatomy.

3 Results

3.1 Planar blast waves of Friedlander type

Figure 4 shows the measured incident (side-on) pressures at various locations along the length of the shock tube. The sensors A, B, C are mounted on the shock tube (marked on Fig. 1a) and located at distances of 1,911, 2,654, and 3,124 mm, respectively, from the driver section. Sensor A is located immediately after the transition section and sensors B and C are in the test section of the shock tube. It can be seen that the shape of shock-blast waveform at sensor A has a flat top with a peak overpressure of 0.27 MPa and positive phase duration of 5.07 ms. The shape of the shock-blast waveform at sensors B and C is of Friedlander type, with peak overpressures of 0.28 and 0.23 MPa and positive phase durations of 5.24 and 5.36 ms, respectively.

3.2 Mechanics of blast wave–head interactions

The mechanics of the blast wave–head interactions can be studied by monitoring the flow field on the surface of the head. Figure 5a, b, respectively, shows the experimentally measured peak pressures and shock wave velocities on the RED (surrogate) head. Incident pressure is measured at sensor C, and surface pressures are measured at sensor locations shown in Fig. 1c. Incident peak overpressure corresponding to sensor C is 0.23 MPa. The peak surface pressure at location 1 (forehead) is 0.553 MPa, and thus, the pressure amplification (the ratio of reflected pressure to incident pressure) is 2.40 due to fluid–structure interaction effects. The peak surface pressure gradually decreases from locations 1 to 4 as the shock wave traverses the head. The peak pressure at location 5 is higher than the locations 3 and 4. The shock wave velocity at incident blast site also increases over free-field velocity due to fluid–structure interaction effects and then gradually decreases as the shock wave traverses the head. The shock wave velocity between location 3, 4, and 5 falls below the free-field shock wave velocity.

3.3 Comparison of experimental and numerical results

Figure 6 shows the surface pressure–time (p – t) profiles corresponding to sensor locations of Fig. 1c from the shock tube experiment and numerical simulation on the RED (surrogate) head. Experimental pressure–time (p – t) profiles are average over three shots ($N = 3$). There is a good agreement between experiment and numerical simulations, in terms of

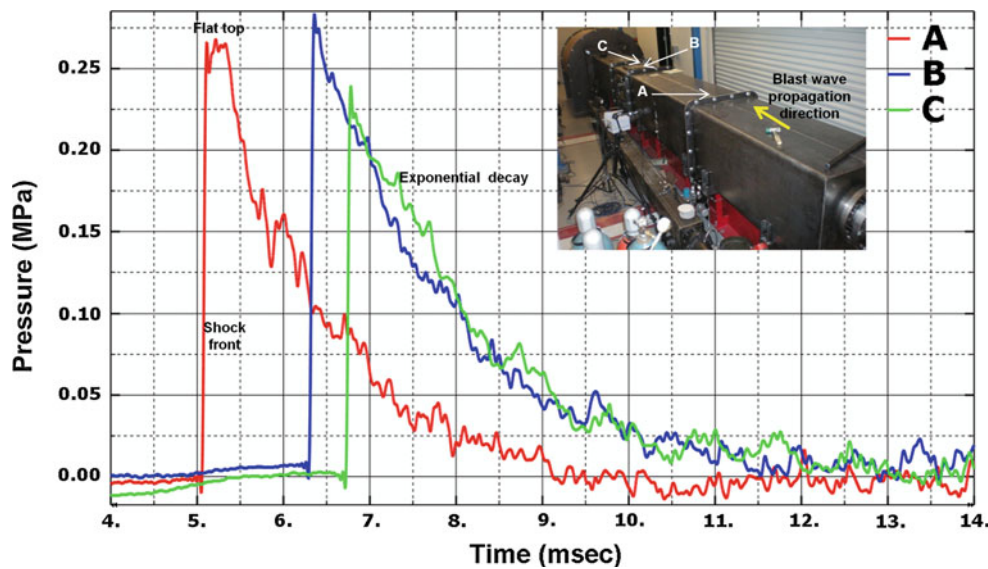


Fig. 4 Blast wave evolution during shock tube experiments

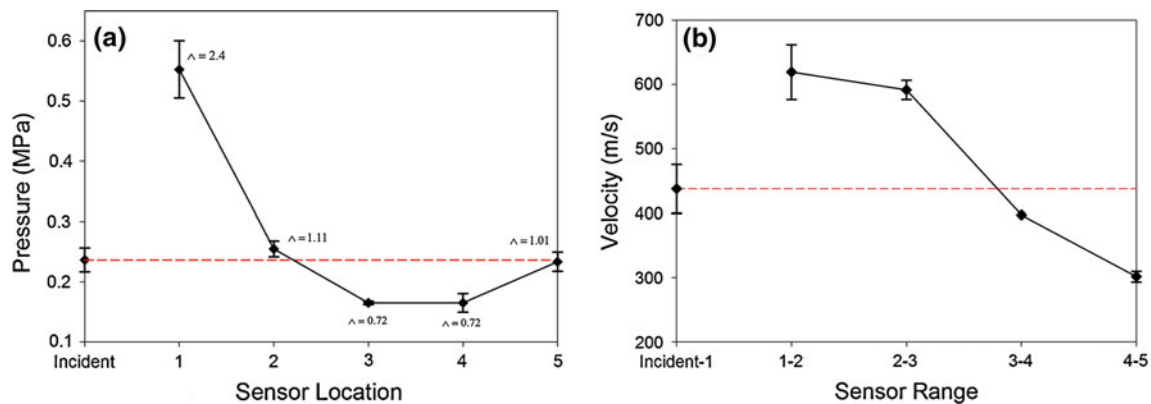


Fig. 5 Mechanics of blast wave head interactions for the surrogate head **a** experimentally measured incident (at sensor C) and surface pressures (corresponding to sensor locations of Fig. 1c) **b** calculated

incident and surface pressure velocities based on arrival times and distance between sensors

peak pressures, nonlinear decay, and positive phase durations. The simulation is able to capture majority of the features well, including the shock front rise time, small peaks and valleys, secondary reflections (e.g. sensors 4 and 5). The arrival times of the experiment are shifted to match arrival times from numerical simulation for ease of comparison of different features of the pressure–time ($p-t$) profile. There is a slight difference in arrival time between the experiment and the numerical simulation of the order of 0.05 ms (50 μ s), at most. Difference in arrival time indicates difference in shock wave speed and does not change the pressure and impulse experienced by the head. The difference in arrival time between experiment and simulation can be attributed to the ideal gas equation of state modeling assumption, membrane rupture pattern, friction along the inner wall of the shock tube, and misinterpretation of the vibrations of the

shock tube itself as pressure readings by the pressure sensors. [Zhu et al. \(2012\)](#) also found similar differences in arrival times from their experiments and numerical simulations due to the reasons stated above.

3.4 Relation between surface pressure, cranial and intracranial stress

In the previous section, we validated the numerical model with experimental measurements for the surrogate head under blast loading conditions wherein the geometry of the surrogate closely matches the anthropometry of a human. In the following sections, the anatomically accurate human head model described in Sect. 2.2 is used not only to understand the surface interactions but also to study the mechanics of load transfer to the brain parenchyma.

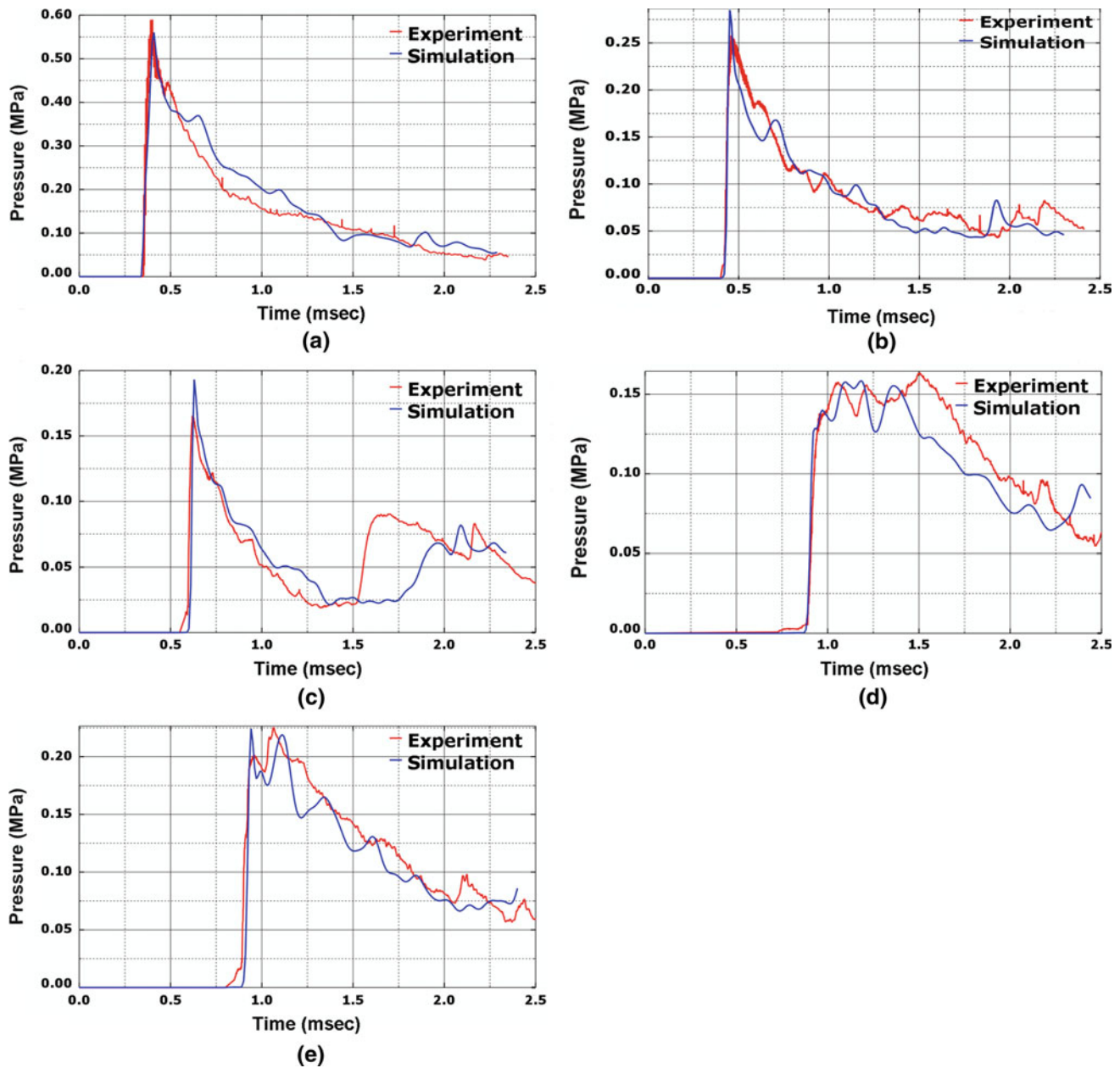


Fig. 6 Comparison of (surface) pressure–time ($p-t$) history from experiment and numerical simulation on the surrogate RED head. **a–e** Represents sensors 1–5, respectively

When the blast wave impacts the head, it gives rise to various types of waves which are defined below.

- (i) **Surface pressure wave:** surface pressure wave is a reflected shock wave on the surface of the head. Surface pressure wave indicates where the shock front is at a given time. In this work, loading induced by the surface pressure wave is considered as a “direct load” as the surface pressure wave transmits energy directly into the brain.

- (ii) **Structural wave in the skull:** when the blast wave impacts the head, it gives rise to a stress wave traveling through the skin, skull, SAS, and brain. Because of its acoustic properties, stress wave in the skull travels much faster than in the other soft tissues of the head. Therefore, the stress wave traveling through the skull is monitored in this work and this wave is defined as a structural wave in the skull. The loading induced by structural wave is considered an “indirect load,” as load is due to structural dynamical deformation.

As the blast is a moving load, the surface pressure loads the skull at different points of time with different intensities from the front to the back. Thus, there will be sequences of direct and indirect loading of the skull and the brain. These direct and indirect loadings cause differential pressure pulses at various regions of the brain differently.

Table 5 shows the arrival times of the surface pressure wave, structural wave in the skull, and pressure wave in the brain corresponding to Sects. 1, 2, 3, 4, and 5 of human head model as shown in Fig. 7. At Sect. 1, the surface pressure wave arrives first which initiates the structural wave in the skull that in turn initiates pressure wave into the brain. At Sect. 2, the structural wave in the skull arrives slightly earlier than the surface pressure wave, since stress wave in the skull travels faster than the surface pressure wave. At Sects. 3, 4, and 5, the structural wave in the skull arrives much earlier than the surface pressure wave. At these sections, the structural wave in the skull establishes a pressure wave in the brain; thus, the pressure wave in the brain also arrives much earlier than the surface pressure wave. This is obvious from the fact that the longitudinal wave speed in the skull is 1,856.79 m/s (Table 2), whereas the surface pressure wave around the head travels at approximately 600 m/s. The free-field blast wave travels at 450 m/s (Fig. 5b).

Figure 7 shows the surface pressures, pressure in the skull, and pressure in the brain at Sects. 1, 2, 3, and 5 of the human head model. As the blast wave encounters the head (Sect. 1), it directly transmits some energy to the brain and at the same time initiates structural wave in the skull. Once this initiation has occurred at Sect. 1, at all other sections, the structural wave arrives earlier than the surface pressure wave, as depicted in Fig. 7. Thus, except for Sect. 1, the initial bio-mechanical loading of the skull and the brain is governed by the structural wave traveling in the skull; when the surface pressure wave arrives at those sections, it causes repressurization in the skull and the brain as shown in Fig. 7. The initial portion of the pressure–time ($p-t$) profile at Sect. 5 in the brain (zoomed in on Fig. 7 and indicated by an asterisk) shows tension (counter-coup pattern), typical of blunt-impact injuries. When the surface pressure (shock) wave arrives at Sect. 5, it induces a compressive load in the brain.

It should also be noted that the pressure profiles of the skull and the brain do not follow surface pressure wave profiles, but instead display oscillating profiles, the potential reasons for the oscillations are elaborated in the discussion section.

3.5 Deformation of the skull

The blast wave continues to impose load on various segments of the skull, as it traverses from the front to back. At the same time, the stress wave travels through the skull at a speed faster than the blast wave causing complex changes in the shape of the skull. Shape changes of the skull are

Table 5 Arrival times of the surface pressure wave, structural wave in the skull and pressure wave in the brain at marked sections of Fig. 7

Section	Arrival time (ms)		
	Surface pressure wave	Structural wave in the skull	Pressure wave in the brain
1	0.35	0.37	0.39
2	0.41	0.40	0.43
3	0.58	0.47	0.51
4	0.73	0.52	0.56
5	0.85	0.55	0.59

studied by monitoring transverse displacement of the skull in the mid-axial plane. Figure 8 shows vector plots of the skull (shell, from here on) transverse displacement at various times. The motion of the shell is considered inward or outward with respect to its position at an earlier time frame. Initially ($t = 0.51$ ms), the frontal portion of the shell moves inward and the portion adjacent to it moves outward; at this time, the stress wave has not propagated into the back of the shell. At slightly later time ($t = 0.59$ ms), the stress wave propagates into the back of the shell. At this time, the front and back portions of the shell moves inward and the center portion moves outward. As time progresses, the central portion of the shell starts moving inward ($t = 0.69$ ms) and eventually a majority of the shell points inward with respect to longitudinal axis ($t = 0.82$ ms). This is followed by the front portion of the shell moving outward, while the center and back portions continue to move inward ($t = 0.89$ ms). At further times, the center and back portions of the shell also starts moving outward ($t = 1$ ms and $t = 1.07$ ms) and eventually a majority of the shell points outward with respect to the longitudinal axis ($t = 1.43$ ms). This is followed by the entire shell moving inward (with respect to previous positions) but at a differential rate; the front and the center portions move faster than the back portion of the shell ($t = 1.92$ ms and $t = 2.14$ ms). Then, the shell tries to equilibrate to its original shape ($t = 2.36$ ms and $t = 2.50$ ms). These vector plots clearly indicate that shell oscillates along the longitudinal axis, and differential motion of various portions of the shell causes the flexing (bending) of the shell. In addition to monitoring transverse displacement, radial (ε_{rr}) and circumferential ($\varepsilon_{\theta\theta}$) strains are also analyzed at various locations of the shell (plots not shown for brevity). A local cylindrical coordinate system is used at each location. It is found that $\varepsilon_{\theta\theta}$ is ~ 10 times higher than ε_{rr} and this confirms that the complex deformations cause flexing of the shell. As the shell stiffness is increased, both ε_{rr} and $\varepsilon_{\theta\theta}$ are significantly reduced causing a reduction in the stresses observed in the brain (results not shown for brevity).

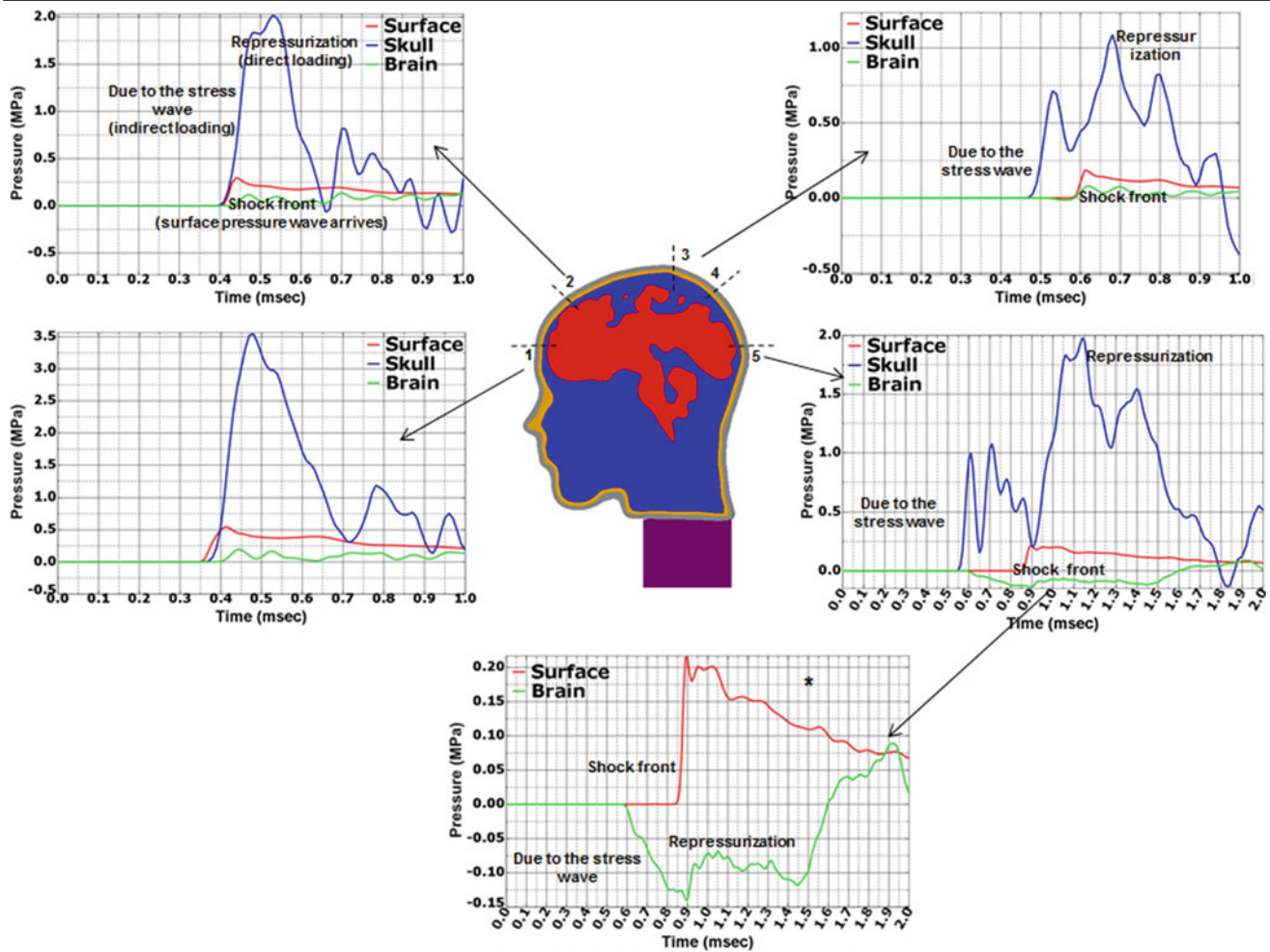


Fig. 7 Relationship between surface pressure, cranial and intracranial stress

3.6 Pressure field inside the brain

One of the important information in studying the effect of blast wave on the occurrence of TBI is in understanding how pressure varies within the brain as a function of space and time. Though we have used pressure as the metric to evaluate the damage state, other parameters like strain may serve this purpose. However, it is much easier to measure pressure in the fluidic brain compared to strain. Figure 9 shows the pressure profile along the centerline of the brain in the mid-sagittal plane. This section is selected as a representative section to understand the effects of loadings due to surface pressures and structural dynamical deformations, and the resulting pressure evolutions in the brain. Various locations at which the pressure history is plotted are marked. Pressure profiles at location 1 and location 6 show typical coup (compression)-countercoup (tension) pattern. A tensile wave front (location 6) propagates into the brain from the side opposite to the incident blast side. Thus, there are multiple wave fronts in the brain, a compressive wave front from the incident blast side and a tensile wave front from the side

opposite to the incident blast side. This is further confirmed by arrival timing analysis at locations 3 and 5. The tensile wave arrives at location 5 when the compressive wave arrives at location 3.

Peak pressure at location 1 is ~ 0.165 MPa, and this peak is due to the direct transmission of the blast wave into the brain. The peak is followed by rapid pressure decay; the pressure even goes slightly negative before becoming positive. Pressure in the brain at this location (after the first peak) is governed by wave reflections from various interfaces. The pressure profiles at locations 2–6 are governed by competing effects of the stress wave of the skull, the pressure wave in the brain, wave reflections from the tissue interfaces, and the surface pressure wave. The highest positive pressure (compressive) of 0.303 MPa is observed at location 2. The speed of the longitudinal wave traveling through the brain with brain bulk modulus (K) of 10 MPa is 98.07 m/s, as opposed to $\sim 1,400$ m/s with bulk modulus of 2.19 GPa. Thus, for the case with $K = 10$ MPa, the longitudinal wave travels much slower and hence external blast wave–head interactions and reflections from skull boundaries govern the brain intracra-

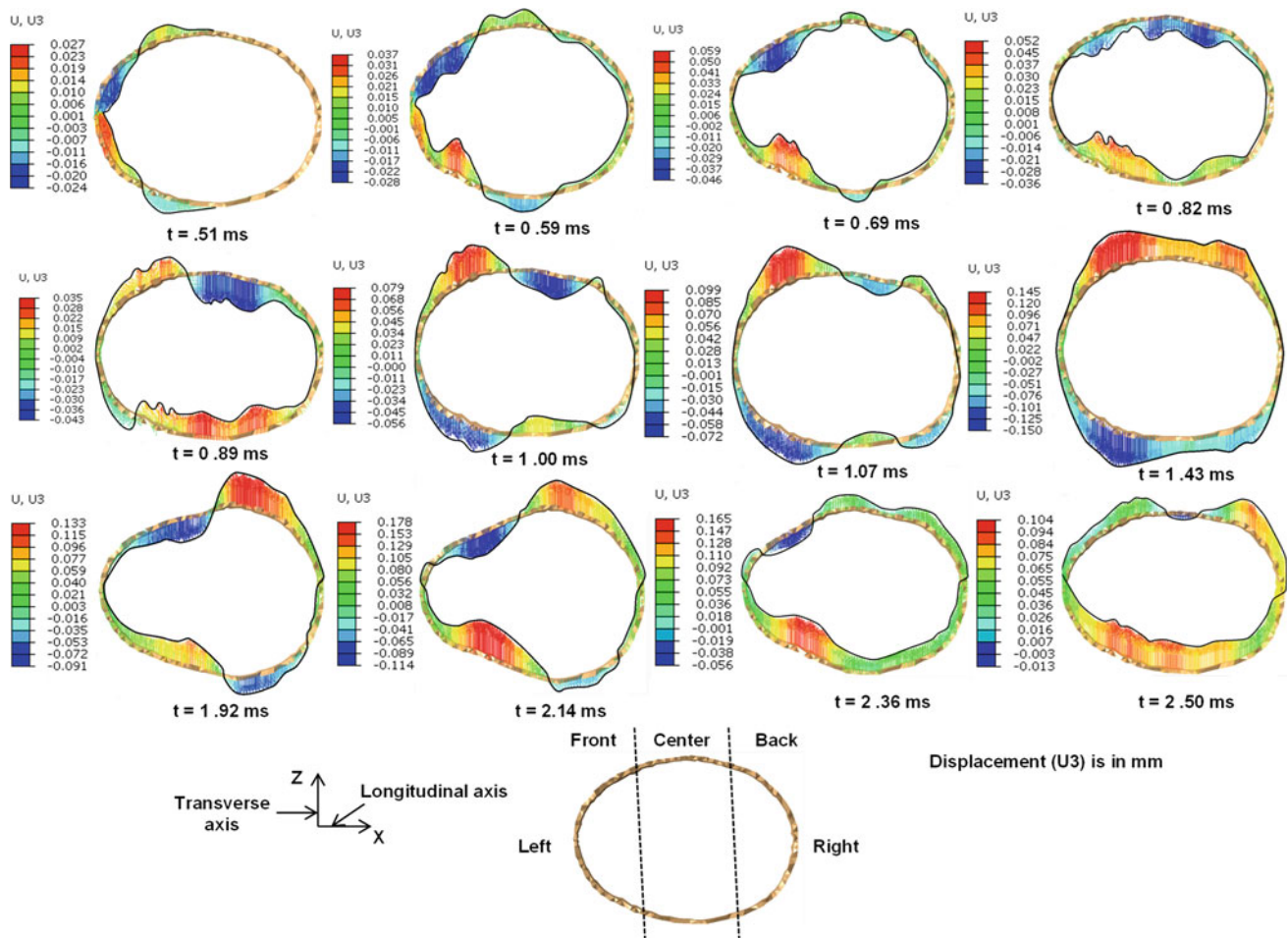


Fig. 8 Deformation of the skull

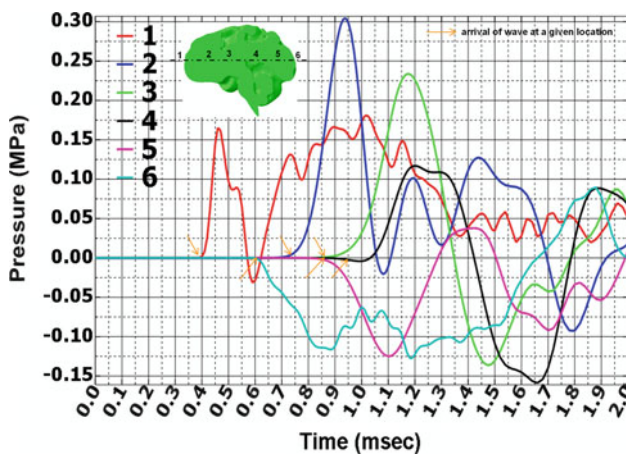


Fig. 9 Pressure field inside the brain

nial pressures. Thus, peak pressure in the brain is observed at location 2 instead of location 1. However, peak pressure in the SAS (0.45 MPa) which is right behind the skull is higher than peak pressure (0.303 MPa) at location 2.

Taylor and Ford (2009) observed the highest pressures in the brain at focal regions located inside the brain due to stress wave action. Grujicic et al. (2011) concluded that multiple reflections give rise to very complex spatial distributions and temporal evolutions of stresses within the brain from their numerical study. Zhu et al. (2010) found highest pressure in the brain at coup site followed by countercoup, top and center. They attributed this pattern to complex wave interactions occurring near the boundaries. Zhu et al. (2012) used validated egg-shaped surrogate model to study the head response under blast loading. Though they have reported highest pressure at coup site, from their data (Figure 18 of the reference), it is clear that the initial impulse (i.e., area under $p-t$ curve) is higher for vertex and center regions as compared to coup location. This corroborates that multiple waves are reaching vertex and center regions. All these studies indicate that intracranial response to the blast wave is governed by the wave interactions. Chen and Ostoj-Starzewski (2010) also observed spherically converging wave pattern at the center of the brain. Pressure profiles at locations 3–6 show a significant amount of negative pressure. Maximum negative pressures

at locations 3, 4, 5, and 6 are -0.13 , -0.16 , -0.12 , and -0.12 MPa, respectively.

4 Discussion

BINT research is yet to identify the exact mechanism(s) in the etiology of the trauma, though a few mechanisms have been suggested. These include: direct cranial transmission (Bauman et al. 2009; Chavko et al. 2007, 2010; Grujicic et al. 2011; Moore et al. 2009; Nyein et al. 2010; Taylor and Ford 2009; Zhu et al. 2012), skull flexure (Bolander et al. 2011; Moss et al. 2009), vasospasm (Bhattacharjee 2008; Cernak 2005b; Cernak et al. 2001; Courtney and Courtney 2009), linear/rotational acceleration (Krave et al. 2005; Zhang et al. 2004), and cavitation (Dogan et al. 1999; Marklund et al. 2001; Nakagawa et al. 2009). Any (or all) of these mechanisms rely on how the external blast energy is transmitted into the various regions of the brain, and how different regions respond to the mechanical insult in the acute, sub-acute and chronic phases. This work has investigated the first part, in relating the external blast load to internal pressures by identifying different biomechanical loading pathways.

An important requirement of this study is the ability to produce repeatable and measurable blast loading conditions that can be related to field conditions that cause actual injury (Cernak 2005a); our blast wave generation facility has been designed and tested to meet this need. The placement of the specimen (surrogate RED head) is contingent upon the desired blast profile (peak overpressure, duration, and impulse) and is typically achieved in the test section (Sundaramurthy et al. 2012). We have also verified that the blast wave is planar at the test section through measurements (Kleinschmit 2011), as this is an important aspect of replicating field conditions.

When the blast wave passes a section of the blast tube, its strength is characterized by a pressure gauge (e.g., PCB, Dyatron, Kulite, Endeveco) measurement mounted on the walls of the tube and is usually referred to as the side-on pressure. This side-on pressure is the incident pressure p_I and measures the static component of the blast wave. Since the velocity component of the pressure wave (dynamic pressure) is not measured by p_I , this does not represent the total energy of the blast. When the blast wave encounters a solid surface, the incident pressure p_I is amplified as the high velocity particles of the shock front are brought to rest abruptly, leading to a reflected pressure p_R on the surface of the body. The amplification factor $\Lambda = \frac{p_R}{p_I}$ (the ratio of reflected pressure to incident pressure) depends on the incident blast intensity, angle of incidence, mass, and geometry of the object and boundary conditions and can vary by a factor of 2–8 for air shocks (Anderson 2001; Ganpule et al. 2011).

The blast-induced biomechanical force on a loaded body (e.g., rats, dummy, human) depends on the reflected pressure and not on the incident pressure. In this work, we pay particular attention to the measurement of reflected surface pressure and hence the imposed biomechanical load on the body. The net biomechanical load F is given by $F = \int_A p_R dA = \int_A \Lambda p_I dA$. Since the amplification factor Λ can vary from 2 to 8 and depends on a number of factors, the force varies across the body even when the incident pressure p_I was to be a constant. Recent experimental studies on rats have shown that surface pressures (and hence the flow field) on the surface of a rat head have significant impact on intracranial pressure (Bolander et al. 2011; Leonardi et al. 2011; Sundaramurthy et al. 2012). Thus, in order to understand flow dynamics around the head, surface pressures and wave velocities are monitored at various locations around the head (Fig. 5). Pressure amplification at the incident blast site (location 1) is $\Lambda = 2.40$ due to reasons stated above. Pressures and shock wave velocities gradually decrease as we move away from the incident blast site. The shock wave velocity in the top and rear region drops below the free-field velocity. The pressure in the top region falls below the incident pressure ($\Lambda = 0.72$ for sensors 3 and 4). The sensor on the back side of the head record a higher pressure than those on the top and this pressure is equivalent to incident pressure ($\Lambda = 1.01$ for sensor 5).

In order to assist in the understanding of this complex flow field, numerical simulations are carried out. From numerical results, it is found that the flow field around the head is governed by the geometry of the head. Significant flow separation is observed on the top and sides (90°) of the head (Fig. 10a). The velocity in the top rear region falls below the free-field velocity due to the flow separation effects. The blast wave traversing the head and the blast wave traversing the neck reunite at the back of the head (Fig. 10b). This reunion causes an increase in pressure on the back side of the head. Several other studies (Chavko et al. 2010; Ganpule et al. 2011; Mott et al. 2008; Taylor and Ford 2009; Zhu et al. 2012) have shown that geometry of the head plays an important role in blast wave–head interactions and the biomechanical loading of the brain. Our results elucidate that the flow dynamics strongly depend on geometry (shape, curvature) and structure (flexural rigidity, thickness) of a specimen and should be considered in understanding biomechanical loading pattern.

The impact of the blast wave with the head at the incident blast site causes a direct load and additionally induces an indirect loading in the form of structural wave traveling through the various head components/tissues. The structural wave through the skull travels faster than any other head component (Table 1) and even faster than the outside surface pressure wave. The surface pressure wave in turn travels faster than the free-field blast wave due to hydrodynamic effects. The structural wave of the skull (indirect loading) governs the initial loading of most of the cranial and intra-

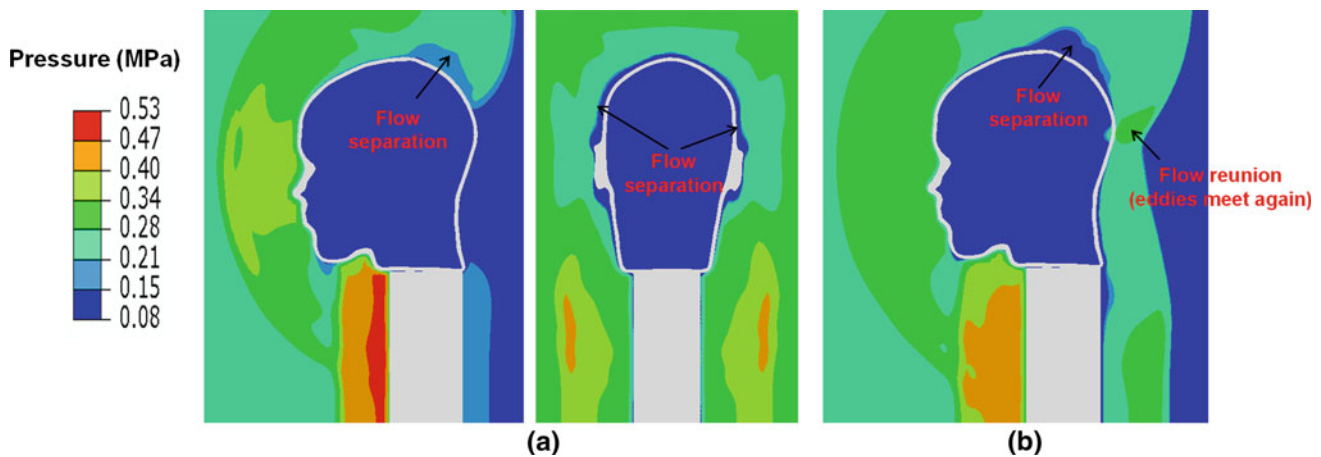


Fig. 10 Flow mechanics around the head as the shock wave traverses the head

cranial contents except the incident blast site region. When the surface pressure wave arrives at given cross-sections, it adds an additional direct load in the form of re-pressurization (Fig. 7). Thus, a blast wave impact even on a small area of the head can trigger the structural wave traveling through the skull, which in turn can induce significant biomechanical loading to the head in the form of an indirect load. Kleinschmit (2011) subjected a cylindrical shell (mimicking the skull) filled with a mineral oil (mimicking the brain) to the blast loading. He measured the surface pressures, surface strains on the shell, and pressures in the mineral oil at various locations and found that the pressure history in the mineral oil is governed by both surface pressures (indicating external blast wave) and surface strains (indicating structural wave and deformation of the skull); our results support his findings. Many of the studies (Bauman et al. 2009; Chavko et al. 2007, 2010; Grujicic et al. 2011; Moore et al. 2009; Nyein et al. 2010; Taylor and Ford 2009; Zhu et al. 2012) on the bTBI have focused on the direct wave transmission aspect of BINT. Our results suggest that in addition to the direct wave transmission effect, structure plays an important role in the biomechanical loading of the brain. If this is the case, then blast mitigation stratagem should not only focus on mitigating the blast wave induced direct loading effects, but should also take into account these structure-induced indirect loading effects.

The pressure profiles in the skull and the brain deviate from surface pressure profiles within a short distance and time. Surface pressure profiles are Friedlander type, whereas pressure profiles in the skull and brain show oscillations (Fig. 7). These oscillations in the pressure profiles can be attributed to several reasons: (1) Presence of the layered system, that is, skin, skull, SAS, brain; wave travel times in the skin, skull, and SAS along the thickness are 23.87, 2.32, and 10.88 μ s, respectively, based on longitudinal wave speed. Thus, the pressure response in the skull and the brain, within a short

time, is degraded by reflections from skin–skull, skull–SAS, and SAS–brain interfaces. (2) The 3D nature of the wave propagation of both structural and surface pressure waves. (3) The surface pressure wave is a moving load; it continuously deforms the skull as it traverses the head, these deformations change the profile.

Any given point, the brain experiences a complex set of direct and indirect loadings emanating from different sources (e.g., reflections from tissue interfaces, skull deformation) at different points of time (Fig. 11). These disturbances continuously propagate into the brain as waves. Constructive and deconstructive interferences of these waves control the pressure–time history in the brain. This is also evident from the pressure profiles along the centerline of the mid-sagittal plane (Fig. 9). Compressive and tensile waves originate from coup (location 1) and countercoup (location 6) sites. Locations 2–5 show a sinusoidal pattern with a change from compression to tension or vice versa, indicating constructive and deconstructive interferences of various waves. The effects of direct and indirect loading on the brain pressure profiles can be delineated only near the surface of the brain (Fig. 7 asterisk) and not deep inside the brain (Fig. 9, locations 2–5). Location 2 (Fig. 9) sees the maximum compressive pressure (0.303 MPa) as the compressive wave front from multiple sources reach this location at the same time. Ward et al. (1980) suggested an intracranial pressure injury index to access brain injury severity and the occurrence of the cerebral contusion. According to them, serious brain injury occurs when peak intracranial pressure (compressive) exceeds 0.235 MPa and minor or no brain injury, for intracranial pressure below 0.173 MPa. If this criterion is applied to our model (Fig. 9), then location 2 exceeds the injury threshold and serious brain injury can occur at location 2. Location 3 records maximum pressure of 0.225 MPa; hence, moderate to serious brain injury can occur at location 3.

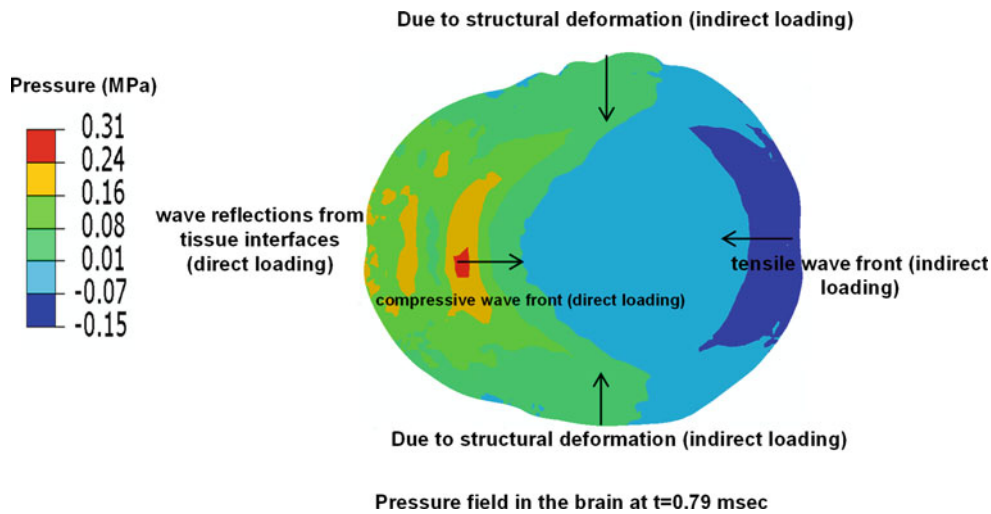


Fig. 11 Wave evolution inside the brain

Skull flexure is proposed as one of the potential mechanisms of brain injury (Moss et al. 2009). The transverse vector displacement plots at the mid-axial section of the skull reveals that the skull oscillates (inward, outward and then equilibrates) about the longitudinal axis at differential rates causing bending or so-called flexure of the skull (Fig. 8). This is further confirmed by circumferential and radial strain analysis; circumferential strains are approximately 10 times larger than radial strains. Bolander et al. (2011) suggested skull flexure as a likely candidate for the development of intracranial pressures from their experimental measurements on rats. A superior rat skull location is identified as the region of the greatest skull flexure. Thus, geometry and thickness of the skull are important parameters that govern intracranial pressures. The detailed understanding of how this skull flexure affects the intracranial pressure is currently being studied (to quantify direct and indirect loading contributions to the intracranial pressure) and will be reported in future communications.

Tissue cavitation is also proposed as another potential mechanism (Dogan et al. 1999; Marklund et al. 2001; Nakagawa et al. 2009). Lubock and Goldsmith (1980) used a spherical shell to resemble the head filled with water to access cavitation theories. They stated that water will form the cavities when exposed to negative pressure below 100 kPa. Locations 3–6 (Fig. 9) exceed this negative pressure threshold; thus, cavitation or microvoid nucleation can occur at these locations, which belong to occipital and midbrain regions. These negative pressures are due to the interaction of different indirect structural waves converging on a point.

Effect of bulk modulus on brain pressure: In order to translate external mechanical load to tissue level kinetic/kinematic parameters, we need anatomically accurate geometric model, precise description of loading/boundary conditions, and valid

material constitutive equations applicable to loading ranges of interest. While significant progress has been made in the former two, the latter remains a challenge. Brain as a whole is very complex with different regions, for example, cerebral cortex, hippocampus, corpus callosum, thalamus, cerebellum, and brain stem to name a few, with their own multi-scale anatomical structures with inherent anisotropy. Being a living matter, the instantaneous behavior can be quite different from the observed behavior in the acute and chronic stages due to the biochemical sequelae that are set in motion following the immediate response due to mechanical stimuli. It is no wonder that Chavko et al. (2010) in their excellent review remark “taken together, the main observation after fifty years of brain tissue investigation is one of huge disparities in the results, especially linked to protocols”. For example, a value of 0.83–2,190 MPa has been used for the bulk modulus of brain. These wide variations in part can be attributed to differences in tissue harvesting procedures, post-mortem testing time, neuroanatomical orientation of the sample, test methods and loading ranges, specimen fixing techniques, data acquisition and interpretation techniques, and last but not the least the animal sources of the tissue itself. Though it is not the purpose of this paper to examine the origin of these variations, here we evaluate the effect of the value of bulk modulus in the present study.

The bulk modulus in the order of MPa to GPa has been used in different research works. In the lower ranges, Claessens et al. (0.83–83.3 MPa) (Claessens et al. 1997), El Sayed et al. (2.19 MPa) (El Sayed et al. 2008), Nahum et al. (4.5 MPa) (Nahum et al. 1977), Belingardi et al. (5.625 MPa) (Belingardi et al. 2005), Zoghi-Moghadam and Sadegh (50 MPa) (Zoghi-Moghadam and Sadegh 2009) have used values in MPas. Values of the order of GPa have been used by Zhang et al. (2.19 GPa) (Zhang et al. 2001a),

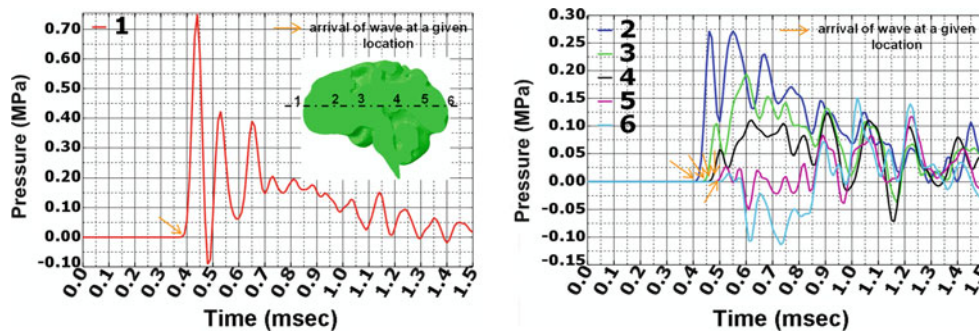


Fig. 12 Pressure field inside the brain for $K = 2.19$ GPa

Willinger et al. [2.19 GPa, but the bulk modulus of subarachnoid space used was low (0.21 MPa)] (Willinger et al. 1999), Takhounts et al. (0.56 GPa) (Takhounts et al. 2008, 2003), Kleiven and von Holst (2.1 GPa) (Kleiven and von Holst 2002). Many of these values were obtained as fitting parameters in computational simulations to match available experimental results of Nahum et al. (1977), though some papers quote previous experimental data (McElhaney et al. 1973; Stalnaker 1969). Ruan et al. (1994) recommended value of bulk modulus between 21.9 and 219 MPa based on parametric studies on three-dimensional finite element head model. Nahum et al. (1977), Ruan et al. (1994), Khalil and Viano (1982), and Nusholtz et al. (1987) have suggested that compressibility of brain tissue is critical in accurately predicting intracranial response. The present work uses a bulk modulus of 10 MPa, based on a recent experimental work by Prevost et al. (2011) conducted on porcine gray/white tissue in unconfined compression under loading/unloading followed by stress relaxation under three different strain rates. The volumetric compliance of the tissue is assessed using video extensometry techniques. The data are combined with experiments of Pervin and Chen (2009) to obtain parameters that are valid over a wide strain rate range ($0.01\text{--}3,000\text{ s}^{-1}$); the authors suggest that this model is suitable for use under impact, blast, and shock loading conditions.

Strain rate for the brain tissue in our simulations is 500 s^{-1} (as opposed to 40 s^{-1} obtained by simulating case 37 of Nahum et al. (1977) impact experiments). This maximum strain rate is observed in frontal region. However, for the sake of understanding the role of the value of bulk modulus in the present study, an additional simulation is conducted with a value of 2.19 GPa and the results are shown in Fig. 12. From the Fig. 12, it can be seen that the higher bulk modulus value leads to increase in peak values of brain pressure as well as shift in the location of maximum peak, due to change in stress magnitudes and wave speeds. The compressive wave front traverses the brain tissue much faster (as can be seen from arrival times) due to change in wave speed and hence effectively erodes the tensile wave front. However, even when bulk modulus value of GPa is used in the simulations, the broader conclusions drawn in the paper remain

unaffected. From the foregoing discussions, it is clear that the value of bulk modulus affects the pressure pattern. Since there is uncertainty in the experimental measuring methods in the evaluation of bulk modulus, these results should be interpreted carefully with this variability in mind.

5 Summary and conclusions

Blast-induced traumatic brain injury is the most prevalent military injury in Iraq and Afghanistan, yet little is known about how blast waves induce brain injury. A comprehensive knowledge of the loading mechanics of brain tissue is important in understanding the pathophysiology of BINT as well as in designing effective mitigation strategies for blast waves. In this work, blast wave–head interactions are studied on dummy and real head models for a frontal blast scenario, using a combined experimental and numerical approach. The critical factors in biomechanical loading of the head-brain complex are identified by understanding the loading pathways of the blast wave from the external surface of the head to the brain. Though this work is primarily focused on planar Friedlander waves (which is important to establish/understand mechanisms), the basic understanding and the results are valid for other complex scenarios of explosion induced blast waves encountered in the field.

Some of the key findings of this work are:

- When a shock-blast wave encounters the head-neck, the flow field around the head is not uniform. Surface pressures and velocities on the surface of the head at incident blast site are amplified due to fluid–structure interactions and hydrodynamic effects.
- Geometry of the head governs the flow dynamics around the head, flow separation and flow reunion; these in turn determine surface pressures and velocities. Surface pressures and shock wave velocities gradually decrease as the blast wave traverses the head. On the back side of the head, a slight increase in surface pressure is observed due to flow reunion.
- Deformation and stress fields in the brain are governed by the surface pressure (external shock) wave and the

structural wave of the skull in terms of direct and indirect loadings, respectively. Structural response plays an important role in the biomechanical loading of the brain.

- Skull deforms in a complex manner at different rates as it oscillates around the brain. These complex deformations are governed by the direct and indirect loadings of the blast that vary with time and can cause flexure (bending) of the skull.
- Pressures in the brain are governed by constructive and deconstructive interferences of various waves reaching a given location in the brain at a given time. It is only possible to delineate effects of direct and indirect loadings near the surface of the brain and not deep inside the brain.
- Occipital and midbrain regions of the brain show a significant amount of negative pressure. Thus, the possibility of cavitation as a potential brain injury mechanism needs to be evaluated.

Acknowledgments The authors acknowledge the financial support provided by the U.S. Army Research Office for the project on “Army-UNL Center for Trauma Mechanics”, Contract No. W91NF-08-1-0483 (Project Manager: Larry Russell, P.I: Namas Chandra). The authors thank Ruqiang Feng, Aaron Holmberg of University of Nebraska–Lincoln (UNL) for many useful discussions.

References

- Anderson J (2001) Fundamentals of aerodynamics. McGraw-Hill, New York
- Baker TJ (2005) Mesh generation: art or science. *Prog Aerosp Sci* 41(1):29–63. doi:[10.1016/j.paerosci.2005.02.002](https://doi.org/10.1016/j.paerosci.2005.02.002)
- Bauman RA, Ling G, Tong L, Januszkiewicz A, Agoston D, Delanerolle N, Kim Y, Ritzel D, Bell R, Ecklund J, Armonda R, Bandak F, Parks S (2009) An introductory characterization of a combat-casualty-care relevant swine model of closed head injury resulting from exposure to explosive blast. *J Neurotrauma* 26(6):841–860. doi:[10.1089/neu.2008.0898](https://doi.org/10.1089/neu.2008.0898)
- Belingardi G, Chiandussi G, Gaviglio I (2005) Development and validation of a new finite element model of human head. In: 19th International technical conference on the enhanced safety of vehicles, Washington, DC
- Bhattacharjee Y (2008) Neuroscience—shell shock revisited: solving the puzzle of blast trauma. *Science* 319(5862):406–408. doi:[10.1126/science.319.5862.406](https://doi.org/10.1126/science.319.5862.406)
- Bolander R, Mathie B, Bir C, Ritzel D, Vandevord P (2011) Skull flexure as a contributing factor in the mechanism of injury in the rat when exposed to a shock wave. *Ann Biomed Eng* 39(10):2550–2559. doi:[10.1007/s10439-011-0343-0](https://doi.org/10.1007/s10439-011-0343-0)
- Bourdin X, Beillas P, Petit P, Troseille X (2007) Comparison of tetrahedral and hexahedral meshes for human finite element modelling: an application to kidney impact. In: 20th Enhanced safety of vehicles conference: innovations for safety: opportunities and challenges
- Cernak I (2005a) Animal models of head trauma. *NeuroRX* 2(3):410–422. doi:[10.1602/neurorx.2.3.410](https://doi.org/10.1602/neurorx.2.3.410)
- Cernak I (2005b) Penetrating and blast injury. *Restor Neurol Neurosci* 23(3):139–143
- Cernak I, Wang ZG, Jiang JX, Bian XW, Savic J (2001) Ultrastructural and functional characteristics of blast injury-induced neuro-trauma. *J Trauma-Injury Infect Crit Care* 50(4):695–706. doi:[10.1097/00005373-200104000-00017](https://doi.org/10.1097/00005373-200104000-00017)
- Chafi M, Karami G, Ziejewski M (2010) Biomechanical assessment of brain dynamic responses due to blast pressure waves. *Ann Biomed Eng* 38(2):490–504. doi:[10.1007/s10439-009-9813-z](https://doi.org/10.1007/s10439-009-9813-z)
- Chandra N, Holmberg A, Feng R (2011) Controlling the shape of the shock wave profile in a blast facility, U.S. Provisional patent application no. 61542354
- Chatelin S, Constantinesco A, Willinger R (2010) Fifty years of brain tissue mechanical testing: from in vitro to in vivo investigations. *Biorheology* 47(5–6):255–276. doi:[10.3233/bir-2010-0576](https://doi.org/10.3233/bir-2010-0576)
- Chavko M, Koller WA, Prusaczyk WK, McCarron RM (2007) Measurement of blast wave by a miniature fiber optic pressure transducer in the rat brain. *J Neurosci Methods* 159(2):277–281. doi:[10.1016/j.jneumeth.2006.07.018](https://doi.org/10.1016/j.jneumeth.2006.07.018)
- Chavko M, Watanabe T, Adeeb S, Lankasky J, Ahlers ST, McCarron RM (2010) Relationship between orientation to a blast and pressure wave propagation inside the rat brain. *J Neurosci Methods* 195(1):61–66. doi:[10.1016/j.jneumeth.2010.11.019](https://doi.org/10.1016/j.jneumeth.2010.11.019)
- Chen Y, Ostojic-Starzewski M (2010) MRI-based finite element modeling of head trauma: spherically focusing shear waves. *Acta Mech* 213(1–2):155–167. doi:[10.1007/s00707-009-0274-0](https://doi.org/10.1007/s00707-009-0274-0)
- Cifuentes AO, Kalbag A (1992) A performance study of tetrahedral and hexahedral elements in 3-D finite element structural analysis. *Finite Elem Anal Des* 12(3–4):313–318. doi:[10.1016/0168-874x\(92\)90040-j](https://doi.org/10.1016/0168-874x(92)90040-j)
- Claessens M, Sauren F, Wismans J (1997) Modeling of the human head under impact conditions: a parametric study. In: Proceedings of 41st stapp car crash conference, pp 315–328
- Courtney AC, Courtney MW (2009) A thoracic mechanism of mild traumatic brain injury due to blast pressure waves. *Med Hypotheses* 72(1):76–83. doi:[10.1016/j.mehy.2008.08.015](https://doi.org/10.1016/j.mehy.2008.08.015)
- DePalma RG, Burris DG, Champion HR, Hodgson MJ (2005) Blast injuries. *N Engl J Med* 352(13):1335–1342. doi:[10.1056/NEJMr042083](https://doi.org/10.1056/NEJMr042083)
- Desmoulin GT, Dionne JP (2009) Blast-induced neurotrauma: surrogate use, loading mechanisms, and cellular responses. *J Trauma-Injury Infect Crit Care* 67(5):1113–1122. doi:[10.1097/TA.0b013e3181bb8e84](https://doi.org/10.1097/TA.0b013e3181bb8e84)
- Dogan A, Rao AM, Baskaya MK, Hatcher J, Temiz C, Rao VLR, Dempsey RJ (1999) Contribution of polyamine oxidase to brain injury after trauma. *J Neurosurg* 90(6):1078–1082. doi:[10.3171/jns.1999.90.6.1078](https://doi.org/10.3171/jns.1999.90.6.1078)
- El Sayed T, Mota A, Fraternali F, Ortiz M (2008) Biomechanics of traumatic brain injury. *Comput Methods Appl Mech Eng* 197(51–52):4692–4701. doi:[10.1016/j.cma.2008.06.006](https://doi.org/10.1016/j.cma.2008.06.006)
- Elder GA, Cristian A (2009) Blast-related mild traumatic brain injury: mechanisms of injury and impact on clinical care. *Mount Sinai J Med* 76(2):111–118. doi:[10.1002/msj.20098](https://doi.org/10.1002/msj.20098)
- Ganpule S, Gu L, Alai A, Chandra N (2011) Role of helmet in the mechanics of shock wave propagation under blast loading conditions. *Comput Methods Biomech Biomed Eng* 1–12. doi:[10.1080/10255842.2011.597353](https://doi.org/10.1080/10255842.2011.597353)
- Grujicic M, Bell W, Pandurangan B, Glomski P (2011) Fluid/structure interaction computational investigation of blast-wave mitigation efficacy of the advanced combat helmet. *J Mater Eng Perform* 20(6):877–893. doi:[10.1007/s11665-010-9724-z](https://doi.org/10.1007/s11665-010-9724-z)
- Honma H, Ishihara M, Yoshimura T, Maeno K, Morioka T (2003) Interferometric CT measurement of three-dimensional flow phenomena on shock waves and vortices discharged from open ends. *Shock Waves* 13(3):179–190. doi:[10.1007/s00493-003-0206-1](https://doi.org/10.1007/s00493-003-0206-1)
- Horgan TJ, Gilchrist MD (2003) The creation of three-dimensional finite element models for simulating head impact biomechanics. *Int J Crashworthiness* 8(4):353–366. doi:[10.1533/tjcr.2003.0243](https://doi.org/10.1533/tjcr.2003.0243)
- Jiang Z, Wang C, Miura Y, Takayama K (2003) Three-dimensional propagation of the transmitted shock wave in a square cross-

- sectional chamber. *Shock Waves* 13(2):103–111. doi:10.1007/s00193-003-0197-y
- Kashimura H, Yasunobu T, Nakayama H, Setoguchi T, Matsuo K (2000) Discharge of a shock wave from an open end of a tube. *J Thermal Sci* 9(1):30–36. doi:10.1007/s11630-000-0042-x
- Kennedy EA (2007) The development and validation of a biofidelic synthetic eye for the facial and ocular countermeasure safety (FOCUS) headform. PhD dissertation, Virginia Polytechnic Institute and State University, Blacksburg
- Khalil TB, Viano DC (1982) Critical issues in finite element modeling of head impact. In: Proceedings of 26th stapp car crash conference, SAE Paper No 821150
- Kleinschmit NN (2011) A shock tube technique for blast wave simulation and studies of flow structure interactions in shock tube blast experiments. Master's thesis, University of Nebraska–Lincoln, Lincoln
- Kleiven S, von Holst H (2002) Consequences of head size following trauma to the human head. *J Biomech* 35(2):153–160. doi:10.1016/s0021-9290(01)00202-0
- Krave U, Höjer S, Hansson H-A (2005) Transient, powerful pressures are generated in the brain by a rotational acceleration impulse to the head. *Eur J Neurosci* 21(10):2876–2882. doi:10.1111/j.1460-9568.2005.04115.x
- Leonardi AD, Bir CA, Ritzel DV, VandeVord PJ (2011) Intracranial pressure increases during exposure to a shock wave. *J Neurotrauma* 28(1):85–94. doi:10.1089/neu.2010.1324
- Ling G, Bandak F, Armonda R, Grant G, Ecklund J (2009) Explosive blast neurotrauma. *J Neurotrauma* 26(6):815–825. doi:10.1089/neu.2007.0484
- Lubock P, Goldsmith W (1980) Experimental cavitation studies in a model head–neck system. *J Biomech* 13(12):1041–1052. doi:10.1016/0021-9290(80)90048-2
- Marklund N, Clausen F, Lewen A, Hovda DA, Olsson Y, Hillered L (2001) Alpha-Phenyl-tert-N-butyl nitron (PBN) improves functional and morphological outcome after cortical contusion injury in the rat. *Acta Neurochirurgica* 143(1):73–81. doi:10.1007/s007010170141
- McElhaney J, Melvin JW, Roberts VL, Portnoy HD (1973) Dynamic characteristics of the tissues of the head. In: Kenedi RM (ed) Perspectives in biomedical engineering. Macmillian Press Ltd, London, pp 215–222
- Moore DF, Radovitzky RA, Shupenko L, Klinoff A, Jaffee MS, Rosen JM (2008) Blast physics and central nervous system injury. *Future Neurol* 3(3):243–250. doi:10.2217/14796708.3.3.243
- Moore DF, Jerusalem A, Nyein M, Noels L, Jaffee MS, Radovitzky RA (2009) Computational biology—modeling of primary blast effects on the central nervous system. *Neuroimage* 47:T10–T20. doi:10.1016/j.neuroimage.2009.02.019
- Moss WC, King MJ, Blackman EG (2009) Skull flexure from blast waves: a mechanism for brain injury with implications for helmet design. *Phys Rev Lett* 103:10–108702. doi:10.1103/PhysRevLett.103.108702
- Mott DR SD, Young TR, Levine J, Dionne JP, Makris A, Hubler G (Sept 1st–5th 2008) Blast-induced pressure fields beneath a military helmet. In: 20th international symposium on military aspects of blast and shock, Oslo
- Nahum A, Smith R, Ward C (1977) Intracranial pressure dynamics during head impact. In: Proceedings of 21st stapp car crash conference, pp 339–366
- Nakagawa A, Fujimura M, Kato K, Okuyama H, Hashimoto T, Takayama K, Tomimaga T (2009) Shock wave-induced brain injury in rat: novel traumatic brain injury animal model *Acta Neurochirurgica Supplements*. In: Steiger HJ (ed) *Acta neurochirurgica supplementum*, vol 102. Springer, Vienna, pp 421–424. doi:10.1007/978-3-211-85578-2_82
- National Institutes of Health (2009) The Visible Human Project, National Library of Medicine, http://www.nlm.nih.gov/research/visible/visible_human.html
- Nicolle S, Lounis M, Willinger R, Palierne JF (2005) Shear linear behavior of brain tissue over a large frequency range. *Biorheology* 42(3):209–223
- Nusholtz GS, Kaiker PS, Gould WS (1987) Two factors critical in the pressure response of the impacted head. *Aviat Space Environ Med* 58(12):1157–1164
- Nyein MK, Jason AM, Yu L, Pita CM, Joannopoulos JD, Moore DF, Radovitzky RA (2010) In silico investigation of intracranial blast mitigation with relevance to military traumatic brain injury. *Proc Natl Acad Sci*. doi:10.1073/pnas.1014786107
- Pervin F, Chen WW (2009) Dynamic mechanical response of bovine gray matter and white matter brain tissues under compression. *J Biomech* 42(6):731–735. doi:10.1016/j.jbiomech.2009.01.023
- Prevost TP, Balakrishnan A, Suresh S, Socrate S (2011) Biomechanics of brain tissue. *Acta Biomaterialia* 7(1):83–95. doi:10.1016/j.actbio.2010.06.035
- Ramos A, Simões JA (2006) Tetrahedral versus hexahedral finite elements in numerical modelling of the proximal femur. *Med Eng Phys* 28(9):916–924. doi:10.1016/j.medengphy.2005.12.006
- Ruan JS, Khalil T, King AI (1994) Dynamic response of the human head to impact by three-dimensional finite element analysis. *J Biomech Eng Trans ASME* 116(1):44–50
- Schneiders R (2000) Algorithms for quadrilateral and hexahedral mesh generation. In: Proceedings of the VKI lecture series on computational fluid dynamics
- Stalnaker RL (1969) Mechanical properties of the head, Ph.D. Dissertation. West Virginia University
- Sundaramurthy A, Alai A, Ganpule S, Holmberg A, Plougonven E, Chandra N (2012) Blast-induced biomechanical loading of the rat: experimental and anatomically accurate computational blast injury model. *J Neurotrauma* [ahead of print. doi:10.1089/neu.2012.2413]
- Takhounts EG, Eppinger RH, Campbell JQ, Tannous RE, Power ED, Shook LS (2003) On the development of the SIMon finite element head model. *Stapp Car Crash J* 47:107–133
- Takhounts EG, Ridella SA, Hasija V, Tannous RE, Campbell JQ, Malone D, Danelson K, Stitzel J, Rowson S, Duma S (2008) Investigation of traumatic brain injuries using the next generation of simulated injury monitor (SIMon) finite element head model. *Stapp Car Crash J* 52:1–31
- Tanielian T, Jaycox LH (2008) Invisible wounds of war. RAND Corp, Santa Monica
- Taylor PA, Ford CC (2009) Simulation of blast-induced early-time intracranial wave physics leading to traumatic brain injury. *J Biomech Eng Trans ASME* 131(6):061007. doi:10.1115/1.3118765
- Teasdale G, Jennett B (1974) Assessment of coma and impaired consciousness: a practical scale. *Lancet* 304(7872):81–84. doi:10.1016/s0140-6736(74)91639-0
- Trosseille X, Tarrière C, Lavaste F, Guillon F, Domont A (1992) Development of a F.E.M. of the human head according to a specific test protocol. SAE Technical Paper 922527. In: Stapp car crash conference. doi:10.4271/922527
- Wang Y, Wei YL, Oguntayo S, Wilkins W, Arun P, Valiyaveetil M, Song J, Long JB, Nambiar MP (2011) Tightly coupled repetitive blast-induced traumatic brain injury: development and characterization in mice. *J Neurotrauma* 28(10):2171–2183. doi:10.1089/neu.2011.1990
- Ward CC, Chan M, Nahum AM (1980) Intracranial pressure—a brain injury criterion. In: Proceedings of 24th stapp car crash conference SAE No. 801304, p 161

- Wieding J, Souffrant R, Fritsche A, Mittelmeier W, Bader R (2012) Finite element analysis of osteosynthesis screw fixation in the bone stock: an appropriate method for automatic screw modelling. *PLoS One* 7(3):e33776. doi:[10.1371/journal.pone.0033776](https://doi.org/10.1371/journal.pone.0033776)
- Willinger R, Kang HS, Diaw B (1999) Three-dimensional human head finite-element model validation against two experimental impacts. *Ann Biomed Eng* 27(3):403–410. doi:[10.1114/1.165](https://doi.org/10.1114/1.165)
- Zhang L, Yang KH, Dwarampudi R, Omori K, Li T, Chang K, Hardy WN, Khalil TB, King AI (2001a) Recent advances in brain injury research: a new human head model development and validation. *Stapp Car Crash J* 45:369–394
- Zhang LY, Yang KH, King AI (2001b) Comparison of brain responses between frontal and lateral impacts by finite element modeling. *J Neurotrauma* 18(1):21–30. doi:[10.1089/089771501750055749](https://doi.org/10.1089/089771501750055749)
- Zhang LY, Yang KH, King AI (2004) A proposed injury threshold for introduction mild traumatic brain injury. *J Biomech Eng Trans ASME* 126(2):226–236. doi:[10.1115/1.1691446](https://doi.org/10.1115/1.1691446)
- Zhu F, Mao H, DalCengio Leonardi A, Wagner C, Chou C, Jin X, Bir C, VandeVord P, Yang KH, King AI (2010) Development of an FE Model of the rat head subjected to air shock loading. *Stapp Car Crash J* 54:211–225
- Zhu F, Wagner C, DalCengio Leonardi A, Jin X, VandeVord P, Chou C, Yang K, King A (2012) Using a gel/plastic surrogate to study the biomechanical response of the head under air shock loading: a combined experimental and numerical investigation. *Biomech Model Mechanobiol* 11(3–4):341–353. doi:[10.1007/s10237-011-0314-2](https://doi.org/10.1007/s10237-011-0314-2)
- Zoghi-Moghadam M, Sadegh AM (2009) Global/local head models to analyse cerebral blood vessel rupture leading to ASDH and SAH. *Comput Methods Biomech Biomed Eng* 12(1):1–12. doi:[10.1080/10255840802020420](https://doi.org/10.1080/10255840802020420)